

# Gas Assisted Binary Black Hole Formation in AGN Discs

Henry Whitehead<sup>1</sup>\*, Connar Rowan<sup>2</sup>, Tjarda Boekholt<sup>2</sup>, Bence Kocsis<sup>2,3</sup>

<sup>1</sup>*Department of Physics, Astrophysics, University of Oxford, Denys Wilkinson Building, Keble Road, Oxford OX1 3RH, UK*

<sup>2</sup>*Rudolf Peierls Centre for Theoretical Physics, Clarendon Laboratory, University of Oxford, Parks Road, Oxford, OX1 3PU, UK*

<sup>3</sup>*St Hugh's College, St Margaret's Rd, Oxford, OX2 6LE, UK*

22 September 2023

## ABSTRACT

We investigate close encounters by stellar mass black holes (BHs) in the gaseous discs of active galactic nuclei (AGN) as a potential formation channel of binary black holes (BBHs). We perform a series of 2D isothermal viscous hydrodynamical simulations within a shearing box prescription using the Eulerian grid code Athena++. We co-evolve the embedded BHs with the gas keeping track of the energetic dissipation and torquing of the BBH by gas gravitation and inertial forces. To probe the dependence of capture on the initial conditions, we discuss a suite of 345 simulations spanning local AGN disc density ( $\rho_0$ ) and impact parameter ( $b$ ) space. We identify a clear region in  $b - \rho_0$  space where gas assisted BBH capture is efficient. We find that the presence of gas leads to strong energetic dissipation during close encounters between unbound BHs, forming stably bound eccentric BBHs. We find that the gas dissipation during close encounters increases for systems with increased disc density and deeper periapsis passages  $r_p$ , fitting a power law such that  $\Delta E \propto \rho_0^\alpha r_p^\beta$  where  $\{\alpha, \beta\} = \{1.01 \pm 0.04, -0.43 \pm 0.03\}$ . Alternatively, the gas dissipation is approximately  $\Delta E = 4.3 M_d v_H v_p$ , where  $M_d$  is the mass of a single BH minidisc just prior to the encounter when the binary separation is  $2r_H$  (two binary Hill radii),  $v_H$  and  $v_p$  are the relative BH velocities at  $2r_H$  and at the first closest approach, respectively. We derive a prescription for capture which can be used in semi-analytical models of AGN. We do not find the dissipative dynamics observed in these systems to be in agreement with the simple gas dynamical friction models often used in the literature.

**Key words:** binaries: general – transients: black hole mergers – galaxies: nuclei – Hydrodynamics – Gravitational Waves

## 1 INTRODUCTION

Mergers of binary black holes (BBHs) have been detected by ground based observatories LIGO/Virgo/KAGRA by the gravitational waves (GWs) they emit (Abbott et al. 2019). Analysis of these signals reveals a spectrum of black hole (BH) masses that are in tension with stellar evolution models, which predict a limit to BH mass as supernova remnants due to pair-instability (Rakavy & Shaviv 1967). While continual accretion after the BH's initial formation may be sufficient to reach these masses (Safarzadeh & Haiman 2020), an alternative origin for these "mass gap" BHs has been hypothesised to be mergers between BHs (O'Leary et al. 2006, 2016; Gerosa & Berti 2019). Such mergers are expected to occur in dense stellar clusters due to many-body encounters (Mouri & Taniguchi 2002). Outside of stellar clusters, an additional channel for BH merger lies within the gaseous discs surrounding active galactic nuclei (AGN) (McKernan et al. 2012, 2014; Tagawa et al. 2020). In this region we expect a significant number density of BHs within  $\sim 1$ pc (Bahcall & Wolf 1976; Miralda-Escudé & Gould 2000). BHs on orbits inclined to the disc are predicted to be driven into the disc plane by gas dynamical friction, further increasing the likelihood of BH-BH interactions (Bartos et al. 2017; Panamarev et al. 2018).

Binary capture can occur when a sufficient proportion of the binary

energy is dissipated during a close encounter. In planetary/stellar systems this can occur due to tidal deformation of the interacting bodies (Fabian et al. 1975). In the case of BHs, if the encounter is suitably close, GW emission can drive dissipation (Hansen 1972). The requirement for an exceptionally close encounter to drive significant GW dissipation results in a very small capture cross-section by relativistic effects alone (O'Leary et al. 2009), but the likelihood of such a capture occurring is expected to be enhanced during Jacobi interactions where multiple close encounters between BHs can increase the total dissipation (Boekholt et al. 2023a). The presence of gas during a close encounter provides an avenue for binary formation by exerting a drag force through gravitation (gas dynamical friction, Ostriker 1999) or via accretion of gas momentum. In this paper we continue to examine this process using high resolution hydrodynamics simulations.

Previous studies into the formation and evolution of BBHs span a variety of methodologies. Even for studies of BBHs in isolation, the long-term behaviour varies depending on the initial conditions and physics included within. Studies of thicker circumbinary discs with a scale height ratio  $H/R = 0.1$  tend to conclude that binaries should outspiral due to net positive torques (Tang et al. 2017; Muñoz et al. 2019; Moody et al. 2019; Tiede et al. 2020)). This does not seem to hold for studies of cooler, thinner discs (Tiede et al. (2020), Heath & Nixon (2020)), which predict negative net torques. Other simulation specific uncertainties such as choice of resolution, sink rate (Tang

\* E-mail: henry.whitehead@physics.ox.ac.uk

et al. 2017) or softening lengths (Li et al. 2021) also seem to affect the binary evolution. Conclusions drawn by more recent studies seem to have converged towards positive torques softening gaseous BBHs over time, at least for circular equal-mass systems (Muñoz & Lithwick 2020; Duffell et al. 2020; Westernacher-Schneider et al. 2022)). Westernacher-Schneider et al. (2023) suggests that SMBH binaries may possess an electromagnetic signature that could differentiate them from single SMBH quasi-periodic sources due to the eccentric minidisks formed in the binary case.

The situation is complicated further for studies that attempt to analyse the behaviour of BBHs embedded within the shearing flow of an AGN disc. Early numerical simulations suggest that the binary should be hardened by the AGN disc gas during its inward migration (Baruteau et al. 2011), though later studies find that the direction of binary rotation may have an affect, with only binaries rotating in prograde with the AGN disc hardening and retrograde configurations experiencing positive torques (Li et al. 2021). A trio of papers featuring 2D shearing box studies of embedded BBH in AGN found hardening by gas for a range of thermal and viscous properties (Li & Lai 2022, 2023b; Li & Lai 2023a).

More pertinent to this study are investigations into the formation of the BBHs themselves. Numerical methods for these formation events have considered dynamical friction models (DeLaurentiis et al. 2023; Rozner et al. 2023), smoothed-particle hydrodynamics (Rowan et al. 2023b) or Eulerian grid codes (Li et al. 2023). Rowan et al. (2023b) (henceforth CR1) includes study of the subsequent binary evolution and reaches agreement with pre-formed embedded binary studies that hardening is dependent on orbital rotation (prograde/retrograde). CR1 reveals the mechanism for gaseous capture, namely the formations of minidisks around BHs, the importance of the first encounter and how the interplay between the gravitational gas dissipation and accretion determines the outcome. Rowan et al. (2023a, in prep, henceforth CR2) continues this work to consider how the inclusion of gas affects the conclusions of Boekholt et al. (2023a), by probing the interplay between the SMBH effects and gas gravitation/accretion over a wider range of initial conditions.

In this paper, we study the interactions between two initially isolated BHs embedded within an AGN disc using a grid of localised 2D viscous hydrodynamics simulations. We examine how the local density of the AGN disc and the initial radial separation of the BHs affects the likelihood of BBH formation. We perform a total of 345 simulations spanning these two parameters. Compared to previous studies, we provide a finer sampling of parameter space by an order of magnitude, while also testing the capture scenario with a high resolution grid-based hydro method where the gas flow is better resolved. We first describe the computational methodology in Section 2, followed by detailing the system’s initial conditions in Section 3. We present our fiducial model in Section 4, discussing the general chronology of a capture as well as the energetic and angular momentum evolution. We follow this with a broader discussion of simulations with varying initial conditions in Section 5. In Section 6 we describe a novel methodology for predicting the outcome of binary capture without the need for full hydrodynamical simulation, as derived from our numerical models. We discuss the general findings of the investigation in Section 7 and summarise our conclusions in Section 8. Brief asides to specific routines can be found in the Appendices A-G.

## 2 COMPUTATIONAL METHODS

We use the Eulerian GRMHD code Athena++ (Stone et al. 2020) to perform our hydrodynamical simulations. Similar to previous studies (e.g. CR1), we neglect any effects associated with gas self-gravity, relativity, radiation and magnetism, restricting ourselves to an isothermal equation of state for simplicity. We utilise a second-order accurate van Leer predictor-corrector integrator with a piecewise linear method (PLM) spatial reconstruction and Roe’s linearised Riemann solver. A more detailed description of Athena++’s integration, reconstruction and solving routines can be found in Stone et al. (2020). Our simulation tracks a 2D rectangular patch of disc (shearing box) co-rotating at the Keplerian angular frequency  $\Omega$  with respect to the SMBH. The geometry and orientation of this patch are detailed in Figure 1. Within this box our BHs function as Newtonian point masses which are self-consistently propagated through the flow. The natural length scales in the shearing box are the Hill radii of a single BH or BBH ( $r_{H,s}$  and  $r_H$  respectively)

$$r_{H,s} = R \left( \frac{m_{BH}}{3M_{SMBH}} \right)^{\frac{1}{3}}, \quad r_H = R \left( \frac{M_{bin}}{3M_{SMBH}} \right)^{\frac{1}{3}} \quad (1)$$

where  $m_{BH}$  and  $M_{bin}$  are the masses of a single BH or a BBH orbiting a central SMBH of mass  $M_{SMBH}$  at a radius  $R$ .

### 2.1 Gas Dynamics

Due to our rotating frame of reference the gas in the simulation feels, along with the standard hydrodynamical forces, contributions from gravitation towards the stellar mass black holes and inertial forces from the uniform rotation of the shearing box. Evolving the fluid therefore requires solving the extended Navier-Stokes equations:

$$\frac{\partial \rho}{\partial t} + \nabla \cdot (\rho \mathbf{u}) = 0 \quad (2)$$

$$\frac{\partial (\rho \mathbf{u})}{\partial t} + \nabla \cdot (\rho \mathbf{u} \mathbf{u} + P \mathbf{I} + \mathbf{\Pi}) = \rho (\mathbf{a}_{SMBH} - \nabla \phi_{BH}) \quad (3)$$

where we have introduced  $\rho$ ,  $P$ ,  $\mathbf{u}$  and  $\mathbf{\Pi}$  as the gas density, pressure, velocity and viscous stress tensor

$$\Pi_{ij} = \rho \nu \left( \frac{\partial u_i}{\partial x_j} + \frac{\partial u_j}{\partial x_i} - \frac{2}{3} \delta_{ij} \nabla \cdot \mathbf{u} \right) \quad (4)$$

for a kinematic viscosity  $\nu$ , where  $x_i$  are Cartesian position coordinates and  $\delta_{ij}$  is the Kronecker delta, i.e. the  $3 \times 3$  identity matrix. We assume a constant  $\nu$  within our simulation, set by the global  $\alpha$ -disc:  $\nu = \alpha c_s H = \alpha c_s^2 / \Omega$ . See Appendix A for a detailed discussion of this decision. Within the isothermal prescription  $P = c_s^2 \rho$  where the sound speed  $c_s$  is a constant. We have added to the Navier-Stokes equations a term  $\mathbf{a}_{SMBH}$  to account for acceleration of gas due to the central SMBH inducing a rotating frame. This acceleration can be represented in terms of the angular velocity of the frame  $\Omega$  and background shear parameter  $q = d \ln \Omega / d \ln R$ . As our frame is on a Keplerian orbit, we adopt  $q = \frac{3}{2}$ . With this prescription

$$\mathbf{a}_{SMBH} = 2\mathbf{u} \times \Omega \hat{\mathbf{z}} + 2q\Omega^2 \mathbf{x} \quad (5)$$

In this frame there exist equilibrium trajectories  $\mathbf{u}_{eq}$  for which  $\mathbf{a}_{SMBH} = 0$ . These trajectories correspond to circular orbits about the SMBH in the non-rotating inertial frame.

$$\mathbf{u}_{eq} = \begin{pmatrix} 0 \\ -q\Omega \mathbf{x} \end{pmatrix} \quad (6)$$

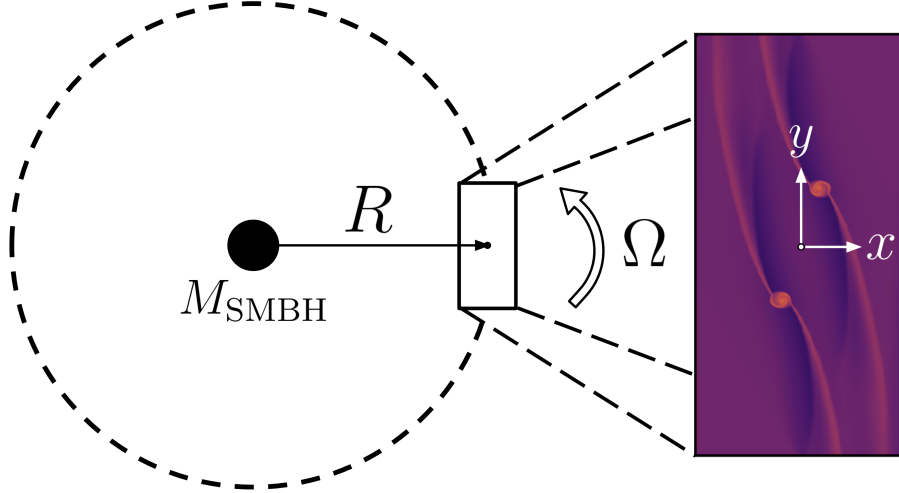


**Figure 1.** Schematic description of the shearing box prescription. Only a Cartesian cut-out of the disc is simulated, in a frame that rotates around the SMBH at the Keplerian rate  $\Omega^2 = GM_{\text{SMBH}}/R^3$ . Pictured within the shearing frame is a generic hydrodynamic snapshot where gas density is displayed with a logarithmic colour map, displaying two BHs approaching each other within their respective minidisks.

Furthermore, there is also contribution from the potential generated by the embedded black holes, which can be expressed as

$$-\nabla\phi_{\text{BH}}(\mathbf{r}) = -G \sum_{n=1}^{n_{\text{BH}}} m_{\text{BH},n} g\left(\frac{\mathbf{r} - \mathbf{r}_n}{d}\right) \quad (7)$$

where  $\mathbf{r}_n$  and  $m_{\text{BH},n}$  are the position and mass of the  $n^{\text{th}}$  BH,  $n_{\text{BH}} = 2$ , and  $d$  is the softening length for the gravitational spline kernel  $g(\delta)$

$$g(\delta) = -\frac{G}{h^2} \delta \begin{cases} \frac{32}{3}\delta - \frac{192}{5}\delta^3 + 32\delta^4 & 0 < \delta \leq \frac{1}{2} \\ -\frac{1}{15\delta^2} + \frac{64}{3}\delta - 48\delta^2 + \frac{192}{5}\delta^3 - \frac{32}{3}\delta^4 & \frac{1}{2} < \delta \leq 1 \\ \frac{1}{\delta^2} & \delta > 1 \end{cases} \quad (8)$$

Here  $h$  is the gravitational smoothing length set to  $h = 0.01r_{\text{h},\text{s}}$  as established in Sec 3.

We do not include the effects of accretion in this study, in part due to the high uncertainties associated with the accretion methodology and rate. CR1 implemented a sink region which conditionally accretes SPH particles near the BHs, finding that accretion is a significant contributor to dissipation. In a follow up study CR2 found that turning off this accretion prompts an increase in gas gravitational dissipation that compensates for the lack of accretion dissipation. Hydrodynamical studies often neglect a physical motivation for the accretion rate within sink regions, or else do not consider how inefficient angular momentum transfer may limit infall near the BHs. We expect that accretion rates close to the BHs should be closely tied to the viscous timescale within these regions. As discussed in Appendix A, the true kinematic viscosity close to each BH is uncertain due to the delicate balance of gravitational and thermal effects. As such, we opt to remove any uncertainty introduced by poorly constrained accretion effects with intent to address accretion with a more developed model in future studies.

We adopt simple outflow boundary conditions in the  $x$  direction (i.e. the radial direction with respect to the SMBH, see Figure 1), but include a refilling routine at the  $y$  boundaries. Refilling involves setting ghost cells to match the properties of the ambient disc. For outflow regions, all ghost cells are set to the values at the domain edge.

No refill is imposed in the  $x$  direction, as the viscous timescale across the domain’s radial extent is much longer than the simulation time. For the  $y$  direction, we impose outflow in “downstream” regions, and refill ambient gas in the “upstream” regions.

$$(y = y_{\text{min}}) = \begin{cases} x < 0 & \text{refill} \\ x \geq 0 & \text{outflow} \end{cases} \quad (9)$$

$$(y = y_{\text{max}}) = \begin{cases} x \leq 0 & \text{outflow} \\ x > 0 & \text{refill} \end{cases} \quad (10)$$

These boundary conditions allow us to ensure minidisc formation does not artificially deplete the shearing box of gas.

## 2.2 Black Hole Dynamics

As each BH perturbs the gas around it gravitationally, they too experience feedback forces to consistently evolve them within the simulation. This is handled by a custom addition to the Athena++ code which tracks and updates the characteristics of  $n$  BHs globally. To ensure that the BH trajectories are properly propagated, we adopt Quinn’s method (Quinn et al. (2010)), specifically designed to integrate equations of motion in the shearing frame where acceleration is a function of both position and velocity. During periods of close encounter, resolving the BH motion requires significantly smaller timesteps than indicated by the Courant-Friedrichs-Lewy (CFL) condition as the BH velocity exceeds that of the local gas. To better set this timescale, we evolve the BHs and gas on a timescale limited by the BH dynamics. This dynamic timescale is set by the minimum of the combined flyby ( $T_{\text{fb}}$ ) and free fall ( $T_{\text{ff}}$ ) timescales for both the BH-BH pair, and the SMBH-BH pairs (e.g. Boekholt et al. 2023b).

$$\Delta t = \eta \min(T_{ij}) \quad T_{ij}^{-4} = T_{\text{fb},ij}^{-4} + T_{\text{ff},ij}^{-4} \quad (11)$$

$$T_{\text{fb},ij}^{-2} = v_{ij}^2 / r_{ij}^2 \quad T_{\text{ff},ij}^{-4} = (GM_{ij})^2 / r_{ij}^6 \quad (12)$$

where  $M_{ij} = m_i + m_j$ ,  $v_{ij} = |\mathbf{v}_i - \mathbf{v}_j|$ ,  $r_{ij} = |\mathbf{r}_i - \mathbf{r}_j|$  are the total mass, relative velocity and separation for BHs  $i$  and  $j$ .  $\eta$  is a scaling prefactor set to 0.001 for stability; the selection method of this value is discussed in Appendix B. When the BHs are distant, the simulation

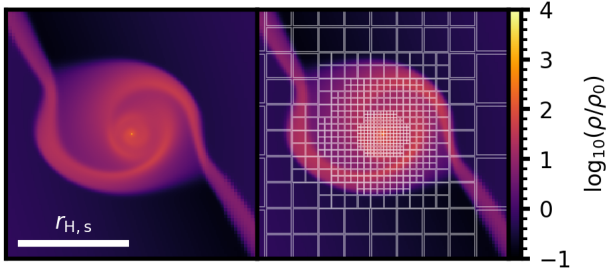


**Figure 2.** Logarithmic density plots of a BH minidisc before close encounter, with a side panel displaying the MeshBlock hierarchy. Each MeshBlock contains  $16 \times 16$  cells: spatially smaller MeshBlocks close to the BH indicate an increase in resolution. There is a step down in refinement outside  $0.2r_{H,s}$  and again at  $0.5r_{H,s}$  where  $r_{H,s}$  is the single Hill radius, see Equation (1). Outside of  $0.5r_{H,s}$ , refinement decreases to the base level while preserving a maximum level difference of 1 between adjacent MeshBlocks.

evolves at a timestep set by the CFL condition and consideration of viscous timescales as handled by Athena++ internally.

Our BHs are initialised within the simulation impulsively at  $t = 0$  yr and do not experience gas gravitation until  $t \approx 6 \Omega^{-1} = 29$  yr when they have formed their own disc and streamers. This is done to reduce the dependency of capture on early disruption to the BH trajectory by asymmetries in the young unstable minidisks. Each simulation will automatically terminate if a BH escapes the domain. BH properties (position, velocity, etc.) are logged every simulation timestep<sup>1</sup>, providing temporally high-resolution data for analysis.

### 2.3 Adaptive Mesh Refinement

Constructing a meshed simulation that is large enough to give each isolated BH time to form a minidisc, while also fine enough to resolve the short length-scale dynamics at close encounter requires mesh refinement: changing the size of cells across the simulation. When using mesh refinement with Athena++, the simulation domain is decomposed into subsections called MeshBlocks, each containing the same number of cells. We implement an add-on to Athena++’s adaptive mesh refinement (AMR) routine, applying progressively higher levels of refinement the closer a MeshBlock is to a BH. Within  $0.2r_{H,s}$  of a BH, the mesh is maximally refined at 6 levels above the root grid. Within the maximum refinement zone the cell size  $\Delta x \sim 0.002r_{H,s}$ . We apply one level less of refinement to MeshBlocks within  $0.5r_{H,s}$  of a BH ( $\Delta x \sim 0.004r_{H,s}$ ). This is demonstrated in Figure 2 where each white outlined MeshBlock contains 256 cells. For a typical timestep before close encounter, this means that  $\sim 65\%$  of all MeshBlocks are within  $0.5r_{H,s}$  of a BH, equivalent to around  $10^5$  cells. For a comparison to previous binary formation studies, Li et al. (2023) utilised a grid code with 50–100 cells per  $r_H$  at maximum resolution; each of our simulations have over 500 cells per  $r_H$  on the highest refinement level. This configuration allows for significantly lower computational expense whilst still adequately resolving the minidisc dynamics and chaotic flows at close encounter, with each individual simulation costing only 60–120 core hours.

<sup>1</sup> Due to storage restrictions, the minimum timestep for BH logging is approximately  $5 \times 10^{-7}$  yr

## 3 INITIAL CONDITIONS

By restricting our study to a small region of the disc, we also simplify our initial conditions. To provide better comparison to CRI, we adopt similar global properties with a Shakura-Sunyaev disc of alpha viscosity  $\alpha = 0.1$ . The shearing box orbits the central SMBH of mass  $M_{\text{SMBH}} = 4 \times 10^6 M_\odot$  at a radial distance  $R = 0.0075$  pc, motivated physically by the pileup of binaries and frequent mergers at these radii observed in the semianalytical models of Tagawa et al. (2020). In principle, we expect the outcome of gas assisted mergers to depend on the mass ratio of the BHs involved, but due to added computational expense associated with expanding the dimensionality of the parameter space we limit ourselves to equal mass interactors with  $m_{\text{BH}} = 25 M_\odot$ . For this BH-SMBH mass ratio, we attain individual and binary Hill radii of  $r_{H,s} = 10^{-4}$  pc and  $r_H = 1.2 \times 10^{-4}$  pc. The simulation domain spans  $0.0015$  pc ( $12.5r_H$ ) radially and  $0.003$  pc ( $25r_H$ ) azimuthally: we then split this domain into a base grid of  $128 \times 256$  cells (128 MeshBlocks). On top of this base mesh, we apply a further 6 levels of AMR, for 7 levels total (see Sec 2.3). In the shearing box we set parameters that would vary in the global disc to constants, namely the disc scale height  $H$ , isothermal sound speed  $c_s$  and kinematic viscosity  $\nu$ . For this study we set  $H/R = 0.005$  to conform to a geometrically thin disc. This scale height then sets  $c_s = H\Omega$ , and  $\nu = \alpha c_s H$ . The density of the ambient flow ( $\rho_0$ ) is treated as a free parameter for this investigation, stated generally in units of  $\rho_* \equiv M_{\text{bin}} r_H^{-3}$ .

The background gas is initialised on a Keplerian orbit with respect to the SMBH, but its velocity field is warped near each BH to reduce chaos in the flows at early times when the BH is suddenly injected (see Appendix C). The BHs are inserted near the  $y$  (or  $\phi$ ) boundary of the shearing box on circular orbits. By starting our simulation when the BHs are distant, they are given enough time to form their own stable minidisks before interacting. They are initially separated azimuthally by  $22^\circ$  and radially by an impact parameter  $b$  which is varied between simulations. Throughout the study,  $b$  is given in units of the binary Hill radius  $r_H$ . The BBH system is initialised such that its centre-of-mass lies in the centre of the shearing box, so as to maximise viable observation time for the interaction. We set the gravitational smoothing length for each BH to  $h = 0.01r_{H,s}$ . We note that gravitational softening is applied only to the BH-gas interactions, the BH-BH interactions feature no softening.

## 4 FIDUCIAL RESULTS

To better understand the dynamics of such complicated systems, we first examine a single fiducial model of a successful gas-assisted capture with initial radial separation  $b = 2.3r_H$  and ambient density  $\rho_0 = 1.9 \times 10^{-4} M_{\text{bin}} r_H^{-3}$ . In this analysis we introduce a series of tools used to describe the hydrodynamic, orbital and energetic evolution of the black holes and their disc environment. In Section 5 we expand the study of these systems by amending parameters in the fiducial model.

### 4.1 Evolution in Isolation

Figure 3 displays the structure of the BH discs before interaction. When the two are far apart, each BH forms its own accretion disc (minidisc). Due to Keplerian shear in the flow, these discs form spiral arms (streamers) that extend inward and outward radially: the

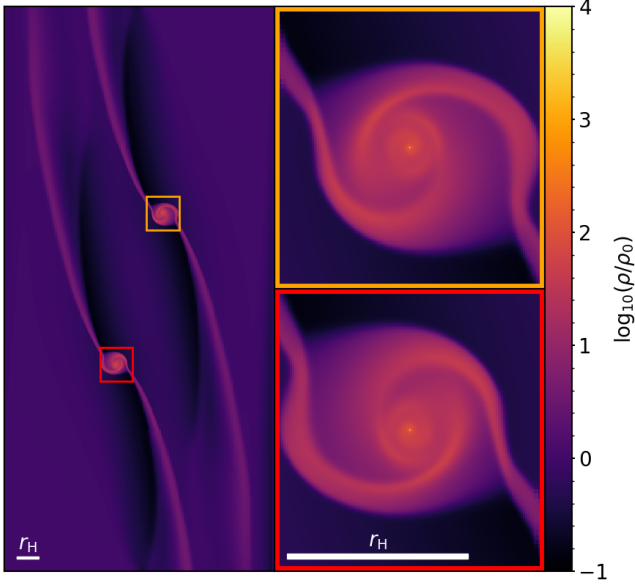


**Figure 3.** Logarithmic density plot of fiducial simulation at  $t \sim 24$ yr with cut-aways for each BH minidisc. Both BHs have formed stable gaseous minidisks with defined spiral structure and strong overdense streamers that propagate across the entirety of the box. Outside the streamers, each BH drives a vacuumation leaving underdense regions in the disc.

inner arm leads the BH orbit, the outer arm lags behind. The BHs are massive enough to drive significant vacuumation in the AGN disc away from these streamers, with  $\rho \sim \rho_0/10$  in the cavities. Each BH initially travels on its equilibrium trajectory in sync with the ambient gas. To avoid perturbation from these trajectories while the discs are forming, we turn off gas gravitational effects on the BH until  $t \sim 29$ yr. As they traverse the azimuthal simulation domain, the BHs gravitate towards each other and begin to distort each other's disc. The BH–BH interaction becomes more significant when they enter each other's mutual Hill sphere at  $t \sim 36$  yr.

## 4.2 Evolution at Capture

Figure 4 displays the evolution of gas density in the vicinity of the two BHs as they approach each other. As the two bodies enter their mutual Hill sphere, their pull is strong enough to deform each other's minidisc and streamers. Once close enough, the streamers interior to the BHs coalesce, forming a bar of shocked gas connecting the two minidisks. The BHs undergo a close encounter at  $t \sim 40$ yr, passing through each other's discs and in doing so dissipating a substantial proportion of their energy to the surrounding gas, leading to the formation of a binary. By depositing orbital energy into the gas, the binary drives significant outflows that strip gas from the inner regions and eject it to the edges of the Hill sphere. There remains sufficient gas in/around the binary to drive further hardening during subsequent periapsis passages, though they are significantly weaker than the first hardening event. The binary components struggle to consistently maintain circumsingle minidisks, as they are disrupted during each periapsis encounter and by interactions with the chaotic circumbinary flow. The evolution described above is consistent with that of Rowan et al. (2023b, Figs. 1 and 3).

## 4.3 Orbital Dynamics

We explore the orbital properties of the binary by means of the eccentricity  $e$  and centre-of-mass (COM) energy  $E_{\text{bin}}$ .

$$e = \sqrt{1 + \frac{2E_{\text{bin}}L_{\text{bin}}^2}{G^2M_{\text{bin}}^2\mu^3}} \quad (13)$$

where we have introduced the binary mass  $M_{\text{bin}} = m_1 + m_2$ , reduced mass  $\mu = m_1m_2/M_{\text{bin}}$  and angular momentum  $L_{\text{bin}} = \mu(\mathbf{r}_1 - \mathbf{r}_2) \times (\mathbf{v}_1 - \mathbf{v}_2)$ . We define  $E_{\text{bin}}$  as the total energy of an isolated binary in its COM frame

$$E_{\text{bin}} = \frac{1}{2}\mu|\mathbf{v}_1 - \mathbf{v}_2|^2 - \frac{GM_{\text{bin}}\mu}{|\mathbf{r}_1 - \mathbf{r}_2|} = -\frac{GM_{\text{bin}}\mu}{2a}. \quad (14)$$

The final equality applies if  $E_{\text{bin}} < 0$ , where  $a$  is the semimajor axis.

In isolation, for two bodies to form a bounded binary they must reduce their total energy such that  $E_{\text{bin}} < 0$ . However when two bodies orbit a third one, the SMBH, the binary separation must remain bounded within  $r_{\text{H}}$  otherwise the tidal and Coriolis forces exerted on the binary may ionise it. The exact boundary for stability within hierarchical triples is dependent on the triple's properties, numerous studies have been made into the functional form of this boundary (Mardling & Aarseth 2001; Vynatheya et al. 2022; Tory et al. 2022). Notably, retrograde binaries are expected to remain stable for larger semimajor axes than prograde (less negative energies), due to the direction of Coriolis acceleration. Within this study, we adopt a single stability threshold for all binaries, requiring that

$$E_{\text{bin}} < \chi E_{\text{H}} \quad (15)$$

where  $\chi = 2$  is a stability parameter set empirically based on the simulations of Tory et al. (2022) and

$$E_{\text{H}} = -\frac{GM_{\text{bin}}\mu}{2r_{\text{H}}} = \frac{a}{r_{\text{H}}}E_{\text{bin}} \quad (16)$$

is the Hill energy: the total energy of a binary with semimajor axis of  $a = r_{\text{H}}$ . This criterion is equivalent to requiring that the binary apoapsis  $r_a$  remain within the binary Hill sphere for all eccentricities  $e < 1$ . We expect the relatively strict  $\chi = 2$  criterion to correctly eliminate the vast majority of unbound systems, while only failing to recognise a small minority of bound systems.

Figure 5 details the evolution of the fiducial binary orbital elements. We mark two times of interest at  $t = 36$ yr and  $t = 39.6$ yr. At the former, the binary energy becomes negative for the first time, indicating the formation of an unstable binary by SMBH tidal forces just after the two BHs enter their mutual Hill sphere. At the latter, a stable binary is formed during the first close encounter, with the binary energy rapidly decreasing due to gas gravitational effects. The binary is highly eccentric, and remains so during the subsequent orbits. While the binary is hard, its high eccentricity results in a relatively large separation at apoapsis where the SMBH tides work most efficiently. This results in oscillations in angular momentum and eccentricity with the same period as the binary. In the following sections we will discuss the mechanism for this binary formation and its subsequent evolution.

## 4.4 Dissipative Effects

To distinguish what phenomena may be attributed specifically to gas dynamics as opposed to the complex behaviour expected of many-body systems, we must quantify how different forces interact energetically with the binary. Work can be done on the binary due to:

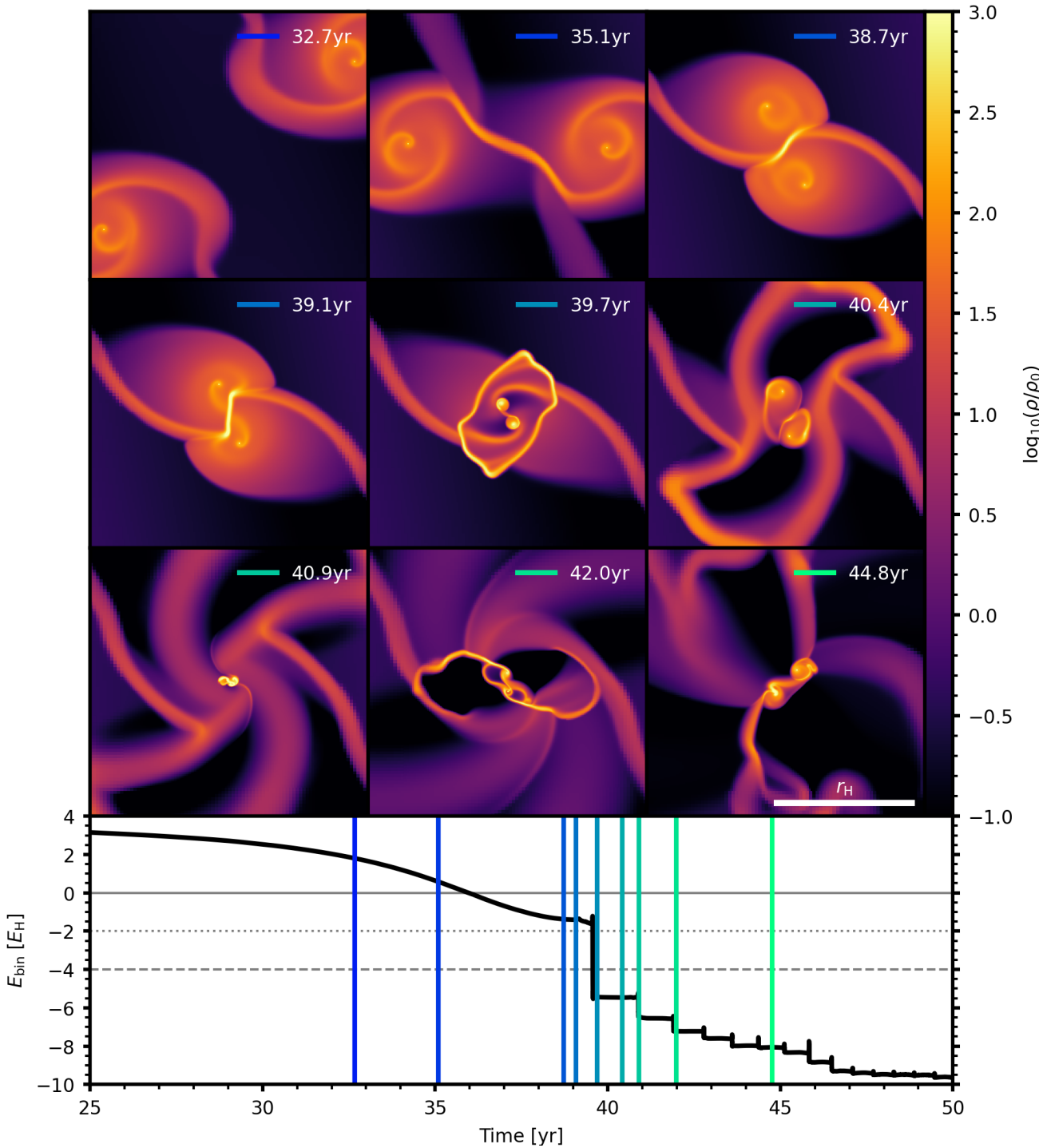


**Figure 4.** Grid of logarithmic density plots for the fiducial simulation at various snapshots from before first encounter to late in the hardening process. Lower panel shows the binary energy in units of the Hill energy  $E_H$ . As the BHs approach periapsis, the two minidisks collide and form a shocked bar of gas. The binary forms during the first close encounter at  $t \sim 40$ yr due to strong gas gravitational dissipation; orbital energy exchanged with the gas disrupts the BH minidisks and partially depletes the mutual Hill sphere of gas. In subsequent periapsis passages, the binary undergoes further impulsive hardening events of lessening strength.

- SMBH forces:  $\epsilon_{\text{SMBH}}$  - each BH experiences centrifugal and Coriolis forces due to the rotating frame, we associate these forces with the central SMBH.
- Gas gravitation:  $\epsilon_{\text{gas}}$  - from differential gravitational gas attraction across the binary components<sup>2</sup>

<sup>2</sup> With accretion neglected, the only dissipation applied to the BBH as a result of gas effects is by BH-gas gravitation

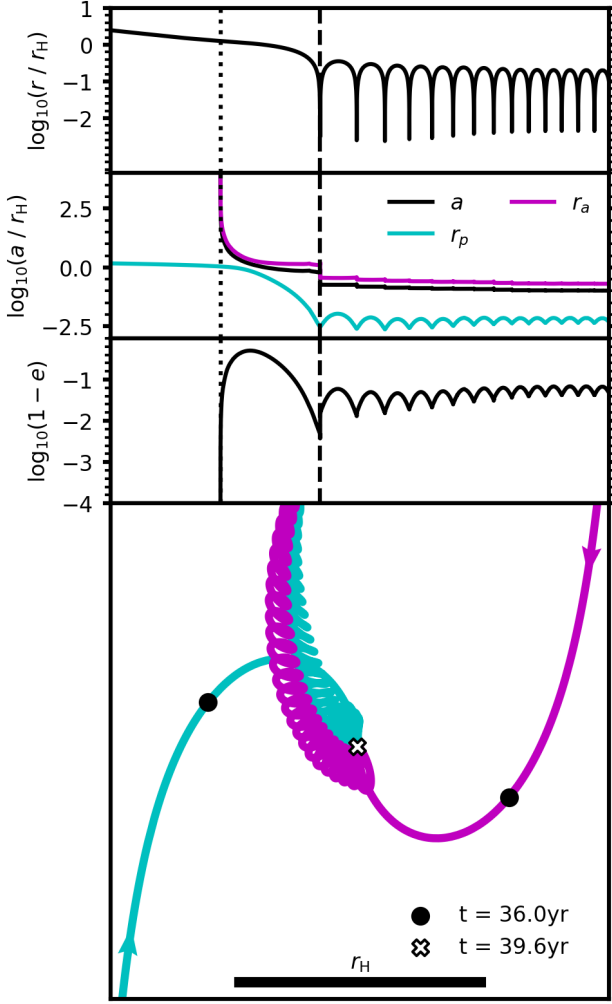


**Figure 5.** Evolution of orbital elements for the fiducial binary system, with the lower panel depicting the trajectories of each of the binary components in the shearing frame. The BHs undergo their first close encounter at 40yr during which gas dissipation results in a stable binary forming. The young binary is knocked away from its equilibrium position and propagates through the shearing box, but the two BHs remain bound together. Torquing by the SMBH results in oscillations in the binary eccentricity on the same period as the binary.

Each of these measures can be calculated from considering the time derivative of the specific binary energy. The full derivation of this quantity is given by Appendix B of CR1.

$$\epsilon = \frac{d}{dt} \left( \frac{E_{\text{bin}}}{\mu} \right) = (\mathbf{v}_1 - \mathbf{v}_2) \cdot (\mathbf{a}_1 - \mathbf{a}_2) \quad (17)$$

We separate the acceleration corresponding to different physical processes as

$$\epsilon_{\text{SMBH}} = (\mathbf{v}_1 - \mathbf{v}_2) \cdot (\mathbf{a}_{1,\text{SMBH}} - \mathbf{a}_{2,\text{SMBH}}) \quad (18)$$

where,  $\mathbf{a}_{\text{SMBH}}$  is expressed in Equation (5), and for the gas gravitation,

$$\epsilon_{\text{gas}} = (\mathbf{v}_1 - \mathbf{v}_2) \cdot (\mathbf{a}_{1,\text{gas}} - \mathbf{a}_{2,\text{gas}}). \quad (19)$$

Here  $\mathbf{a}_{n,\text{gas}}$  is calculated by summing the gravitational attraction on the BH  $n \in \{1, 2\}$  by all  $N_c$  gas cells in the simulation (with masses

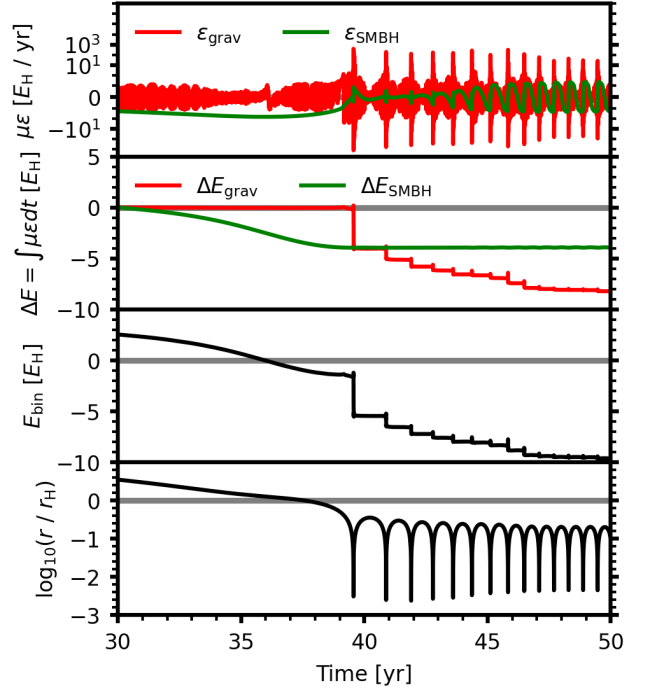


**Figure 6.** Energetic evolution of the fiducial model as the BHs approach first encounter. Upper panel displays variations in the respective binary energy dissipation rate due to the SMBH and gas gravity. The second panel integrates this dissipation over time (starting from  $t = 30\text{yr}$ ) to show the total change in binary energy, which is also obtained directly from the orbital elements in the third panel. The lower panel displays the separation of the binary components. It is clear that close encounters between the black holes are associated with impulsive dissipation events. The SMBH only contributes significant dissipation before the binary is formed at  $t \sim 40\text{yr}$ , after which gas gravitation dominates.

and positions  $m_i$  and  $\mathbf{r}_i$ ).

$$\mathbf{a}_{n,\text{gas}} = G \sum_{i=1}^{N_c} m_i \frac{\mathbf{r}_i - \mathbf{r}_n}{|\mathbf{r}_i - \mathbf{r}_n|^3} \quad (20)$$

Figure 6 details the energetic evolution of the fiducial model with these measures. On approach, energy is steadily extracted from the binary by the SMBH, with gas gravitation being subdominant. Gas gravitation dissipation peaks during the first close encounter, reducing  $E_{\text{bin}}$  by  $\sim 4E_H$  and forming a stable binary. The SMBH continues to do work on the binary, but on smaller magnitudes than gas gravitation and secularly the SMBH's energetic effect averages out to approximately zero once the binary is formed. Gas dissipation continues to peak during subsequent close encounters. The energetic evolution of the bound system follows a clear pattern: impulsive dissipation events at each periapsis harden the binary. As such, the binary energy evolves as an approximate step function, with hardening periods at periapsis but only minor energetic evolution outside of these events. The frequency of these events increase as the binary period shortens, creating a system that rapidly hardens due to gas effects. The following periapsis passages are similarly deep and high velocity to the first, but dissipate significantly less energy: our simulations show that this is likely due to a reduction in gas mass local to the binary as generated by strong outflows during the first periapsis.

The strong localisation of dissipation to periapsis passages can be explained by consideration of the BBH dynamics, the dissipation

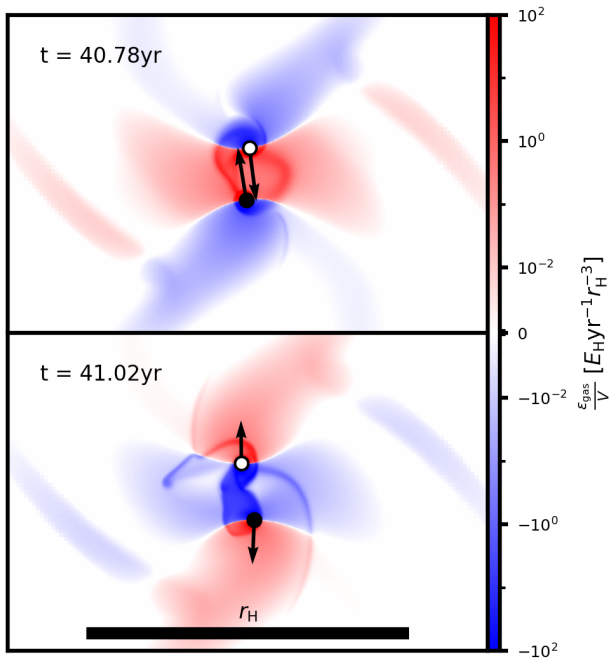


**Figure 7.** Spatial distribution of gravitational gas dissipation density, for the fiducial model before and after a periapsis passage. Highlighted in red are regions of gas injecting energy into the binary (gas leading the orbit), in blue energy is extracted (by gas lagging the orbit). Energy is generally injected on in-fall due to the extra gas mass in the binary system, but extracted as the binary travels towards apoapsis due to minidisc gas being unable to keep up with the binary components. The net effect is a removal of orbital energy from the binary.

equation and the spatial dissipation density distributions. Firstly, for equivalent gas acceleration fields, we expect BBHs with greater relative velocities to dissipate more energy (in Equation (17), velocity is a linear term). We might then question why there is a differential acceleration across the binary components near periapsis. This can be better understood by considering the distribution of gas near the BHs during close encounters. When in isolation, the minidisks are well bound to the BHs and travel with them through the AGN disc. The minidisks collide during close encounters, with the BHs accelerating ahead of their bound gas as they do not feel the same hydrodynamic forces (pressure, viscosity) which generally retard the gas on collision. This leads to a build up of gas behind the BHs and results in a drag force that removes energy from the binary. Figure 7 displays the spatial distribution of dissipation density, where blue regions indicate gas extracting energy from the binary, and red injecting into it. While on in-fall energy injection often exceeds extraction, mass stripped from the minidisc during collision leads to a strong drag after periapsis that results in a net loss of energy. These dissipation events are very short for deep, eccentric flybys as the binary components spend very little time close to periapsis where the gas gravitation is strongest. Neglected from this simulation are the effects of gas self gravity; it is unclear whether introducing an extra acceleration term to the gas would limit or enhance the lagging which drives gas dissipation.

#### 4.5 Torques and Angular Momentum

We can attribute specific torques to the physical processes in a similar method to the definition of dissipation rates in Section 4.4.

$$\boldsymbol{\tau} = \frac{d}{dt} \left( \frac{L_{\text{bin}}}{\mu} \right) = (\mathbf{r}_1 - \mathbf{r}_2) \times (\mathbf{a}_1 - \mathbf{a}_2) \quad (21)$$

$$\boldsymbol{\tau}_{\text{cent}} = (\mathbf{r}_1 - \mathbf{r}_2) \times (\mathbf{a}_{1,\text{SMBH}} - \mathbf{a}_{2,\text{SMBH}}) \quad (22)$$

$$\boldsymbol{\tau}_{\text{gas}} = (\mathbf{r}_1 - \mathbf{r}_2) \times (\mathbf{a}_{1,\text{gas}} - \mathbf{a}_{2,\text{gas}}) \quad (23)$$

Analogous to the Hill energy  $E_H$ , we introduce  $L_H$  as the angular momentum of a circular binary with  $a = r_H$ , such that  $L_H = \mu \sqrt{GM_{\text{bin}} r_H}$ .

Figure 8 details the angular momentum evolution of the fiducial system under these torques. When the BHs are far apart the angular momentum is large and negative with respect to the AGN disc rotation. As the simulation progresses, the angular momentum becomes less negative, driven primarily by the SMBH. There is a  $e < 1$  epoch before true capture during which the BHs are in an unstable binary ( $E_{\text{bin}}/E_H < 2$ ). Following the first encounter when the binary becomes tightly bound, the angular momentum and energy evolution are remarkably different. While the energy continues to decrease during subsequent passages, the angular momentum is nearly constant. Torques by gas gravitation are largely insignificant throughout the evolution, but we might expect gas torques to dominate at late times when the binary has accumulated further gas and SMBH have diminished due to hardening. The binary remains highly eccentric after the first encounter, the eccentricity oscillates between 0.9 and 0.99. As the semimajor axis and apoapsis shrink, the periapsis distance is nearly constant  $r_p \sim 0.003 r_H$  during the evolution. This type of behaviour is opposite to the hierarchical triple evolution without gas, e.g. the eccentric Lidov-Kozai mechanism (Naoz 2016), where  $r_p$  changes at nearly constant  $a$  and it is reminiscent of the evolution for dissipative short-range-interaction processes in highly eccentric binaries such as tidal capture or GW capture.

#### 4.6 Summary of Fiducial Model

The fiducial model builds on previous binary capture studies to provide an independent confirmation for gas-assisted binary formation with different methodologies and systematics. Critically, we extended our model to greater refinement than previous grid-based studies, allowing us to better resolve the chaotic flow structure present in the gas during BH-BH close encounter. The capture is achieved by strong gravitational gas dissipation during the first close encounter. This binding injects substantial energy into the surrounding gas, generating chaotic outflows that strip gas from the minidisks. The binary formed is highly elliptical, and remains so during its subsequent orbits. The SMBH dominates the torque on the binary, forcing oscillations in eccentricity. Post formation binary periapsis passages are accompanied by further hardening events, albeit with minor energy decreases compared to the initial close encounter.

### 5 PARAMETER STUDY

Here we will consider a grid of 345 models generated by amending the initial conditions of our fiducial model (see Section 4). For our base grid, we span the initial ambient disc density approximately uniformly in log space within  $\rho_0 \in [3.3 \times 10^{-5}, 3.3 \times 10^{-3}] M_{\text{bin}} r_H^{-3}$  and impact parameter linearly within  $b \in [1.3, 2.5] r_H$ . We note a difference here to the range of parameters used in **CRI**: in that paper



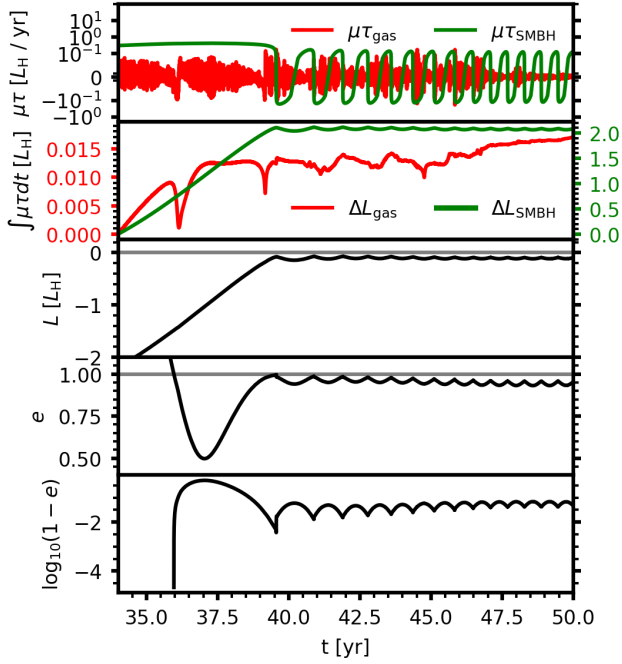


**Figure 8.** Angular momentum evolution for the fiducial model starting from when the black holes are  $1.5r_H$  apart, with panels for instantaneous torques, integrated torques, total binary angular momentum and eccentricity. The angular momentum evolution is dominated by the SMBH throughout.

$r_H$  was the single BH Hill radius, as opposed to the binary Hill radius in this work (Eq. 1). This paper also considers ambient disc densities considerably lower than those analysed in CR1. Compared to previous hydrodynamical studies that generally utilise a few to tens of models (Li et al. 2023), our wide and finely sampled parameter space allows us to better chart the complicated and non-linear nature of the BBH capture environment. The principal “outcome” for each of these simulations concerns the success or failure of binary formation. Achieving a negative binary energy is insufficient to determine long term binding, as SMBH tidal forces may yet ionise the system. A binary capture is considered successful if the binary energy  $E_{\text{bin}}$  is sufficiently negative. As addressed in Section 4.3, the exact boundary for stability is complex, and in this work we take any binary achieving  $E_{\text{bin}} < 2E_h$  to be stable (see Eq. 15). Each simulation terminates once it is sufficiently bound, has become unbound after its initial encounter, or if it reaches  $t = 58\text{yr}$ : this is done to reduce computational cost<sup>3</sup>.

As such, these models provide lots of information about the nature of binary formation, but are not intended to be used for extended study of the resulting binary systems over many orbital periods. This is in part due to the cost of resolving hard binaries, where increasingly small timesteps are required to resolve the BH trajectories accurately (see Appendix B). We expect there to be a minority of cases where a binary identified as unbound at simulation stop may yet harden sufficiently due to gas dissipation to remain bound. Similarly, the empirically derived boundary of  $\chi = 2$  is set by consideration of a large proportion of systems remaining bound beneath this energy; a very small minority of cases may only be quasi-stable. Despite this,

<sup>3</sup> For systems that reach sufficient binding energies or become unbound after first encounter, the system is evolved for a further  $t = \Omega^{-1} \sim 4.84\text{yr}$  to ensure that this is the end state of the system.

we are confident that this observation period allows us to correctly identify the vast majority of binary systems.

## 5.1 Gas-free Interactions

Boekholt et al. (2023a) explored the complex orbital dynamics of a flyby interaction in proximity to a massive companion and identified impact parameters for which arbitrarily close encounters between the flyby bodies could occur. Our initial conditions are slightly different, integrating from an azimuthal separation of  $22^\circ$  instead of a full  $180^\circ$  due to the limited extent of the shearing box. Despite this, we identify many of the same trends, specifically the existence of direct impact trajectories and orbit families associated with different impact parameters. We include here a brief study of the gas-less flyby scenario as test of our integrator and to help inform our understanding of the more complicated response of the system when gas is included. The relationship between impact parameter and periapsis of the first encounter in the gas-less case follows a double-valley shape, with the closest first encounters occurring at  $b \sim 2.0r_H$  and  $2.3r_H$ , respectively. At these impact parameters, the trajectories of the BHs before close encounter lead to maximal angular momentum extraction by the SMBH, resulting in the deepest encounters. For sufficient fine tuning in  $b$ , one can find a trajectory where the BHs pass arbitrarily close to each other. For the initial conditions used in this study, we find these “zero angular momentum” (ZAM) separatrixes near  $b_1 = 1.9975r_H$  and  $b_2 = 2.3225r_H$ . When crossing a separatrix, the sign of angular momentum at periapsis inverts. As such these trajectories mark the edges of families in encounter types, which we label prograde interior, retrograde interior and prograde exterior (PI, RI and PE respectively). Figure 9 describes the nature of these families in the gas-free case, within a frame centred on the inner BH. For  $b < b_1$  (type PI), the outer BH will pass interior to the inner BH with positive angular momentum (prograde with respect to the AGN disk). If the impact parameter is increased slightly, such that  $b_1 < b < b_2$  (type RI), the BH will still pass interior to the inner BH, but now with negative angular momentum (retrograde). Increasing to  $b > b_2$  (type PE), the outer BH will remain exterior to the inner BH at periapsis, on a prograde orbit. For sufficiently small or large impact parameters, the BHs will fail to penetrate their mutual Hill sphere, and no close encounter will occur: for our initial conditions, we only observe mutual Hill sphere penetration for  $1.6625r_H \leq b \leq 2.4375r_H$  in gas-less systems. When gas is introduced to the system, the exact position of these boundaries will move, but understanding the rough relationship between impact parameter, angular momentum extraction by the SMBH and therefore periapsis depth is crucial to interpreting the dissipative effects in the gaseous case, as the depth of first close encounter proves to be strongly correlated with binary formation.

Note that even in the absence of gas, impact parameters close to  $b_1$  and  $b_2$  lead to extremely close encounters that may result in binary formation due to GW emission (or tidal dissipation for stellar encounters): they may even lead to direct head-on collisions in the most fine-tuned case. Boekholt et al. (2023a) describes Jacobi encounters within hierarchical triples as systems where the inner binary experiences multiple close encounters driven by outer body, finding that these encounters occur for specific values of initial impact parameter defined as fractal regions A, B, C. Similar binary capture and direct collision trajectories also exist for subsequent encounters following the first encounter (within regions A, B, C), which increase the total binary capture cross section cumulatively by approximately 25% (Boekholt et al. 2023a). As our initial conditions differ from Boekholt et al. (2023a) the exact boundaries of the Jacobi regions

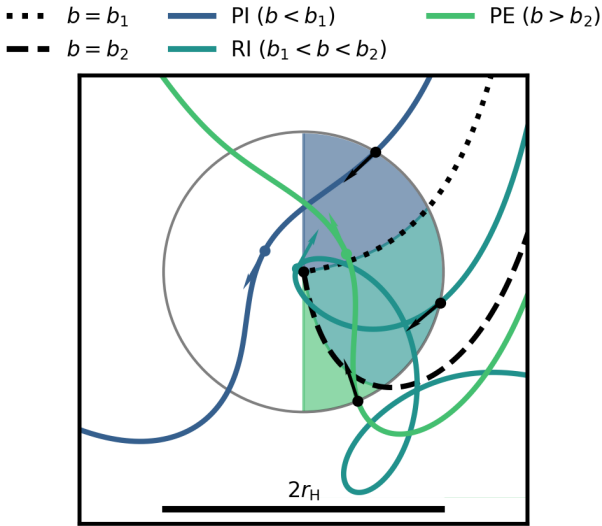


**Figure 9.** BH trajectories in the gas-less case: from a frame centred on the inner BH, each path follows the outer BH. Classes of encounters are identified (prograde internal, retrograde internal and prograde external) by the initially external BH passing inside or outside the inner BH at periaapsis, and in which direction w.r.t the global AGN disc rotation. Each encounter class is separated by a "direct impact" trajectory, at  $b_1 = 1.9975r_H$  or  $b_2 = 2.3225r_H$ . For trajectories with  $b \lesssim 1.6625r_H$  and  $b \gtrsim 2.4375r_H$  we do not expect close encounters to occur in gas-less systems.

are hard to identify, but we can mark their rough positions with respect to the ZAM trajectories. The first wide region A is found at  $b$  values slightly beneath the lower ZAM trajectory at  $b \sim 2.0r_H$ . The next region B is the widest and overlaps with the ZAM trajectory at  $b \sim 2.3r_H$ . The final region C is considerably narrower than the other two and can be found at  $b$  values slightly larger than the  $b \sim 2.3r_H$  ZAM trajectory.

## 5.2 Outcomes

Figure 10 displays the full grid of 345 simulations with gas, spanning a range of initial ambient disc densities and BH impact parameters. A successful binary formation is shaded green, with a failed capture in orange. We note first the high number of captures in this parameter space, despite the relatively low disc densities represented. We see a high number of captures for initial ambient disc densities in excess of  $4 \times 10^{-4} M_{\text{bin}} r_H^{-3}$ . However, within a narrow band of impact parameters around  $b = 2.3r_H$ , we are able to observe successful BBH formation at disc densities of only  $\rho_0 = 10^{-4} M_{\text{bin}} r_H^{-3}$ . We might expect a second narrow band to be present around  $b = 2.0r_H$  due to the deep close encounters predicted here, this discrepancy is discussed in Section 5.4. Secondly, we note that knowledge of either  $\rho_0$  or  $b$  is insufficient to determine the outcome of a close encounter on its own. Thirdly, we observe some failed captures appearing at the highest gas densities and smallest impact parameters (bottom right corner in the figure), as well as a very wide capture section at intermediate densities. These features are discussed in Section 5.5. Understanding the shape of this outcome space requires consideration of the dependency on energy dissipation on both the macro-disc properties and the BH trajectories.

**Table 1.** Best fit parameter values and dispersion ( $\sigma$ ) for the orbital energy dissipated by gas in Eq. (24).

variable	value	$\sigma$
$\log_{10}(A)$	2.63	0.17
$\alpha$	1.01	0.04
$\beta$	-0.43	0.03

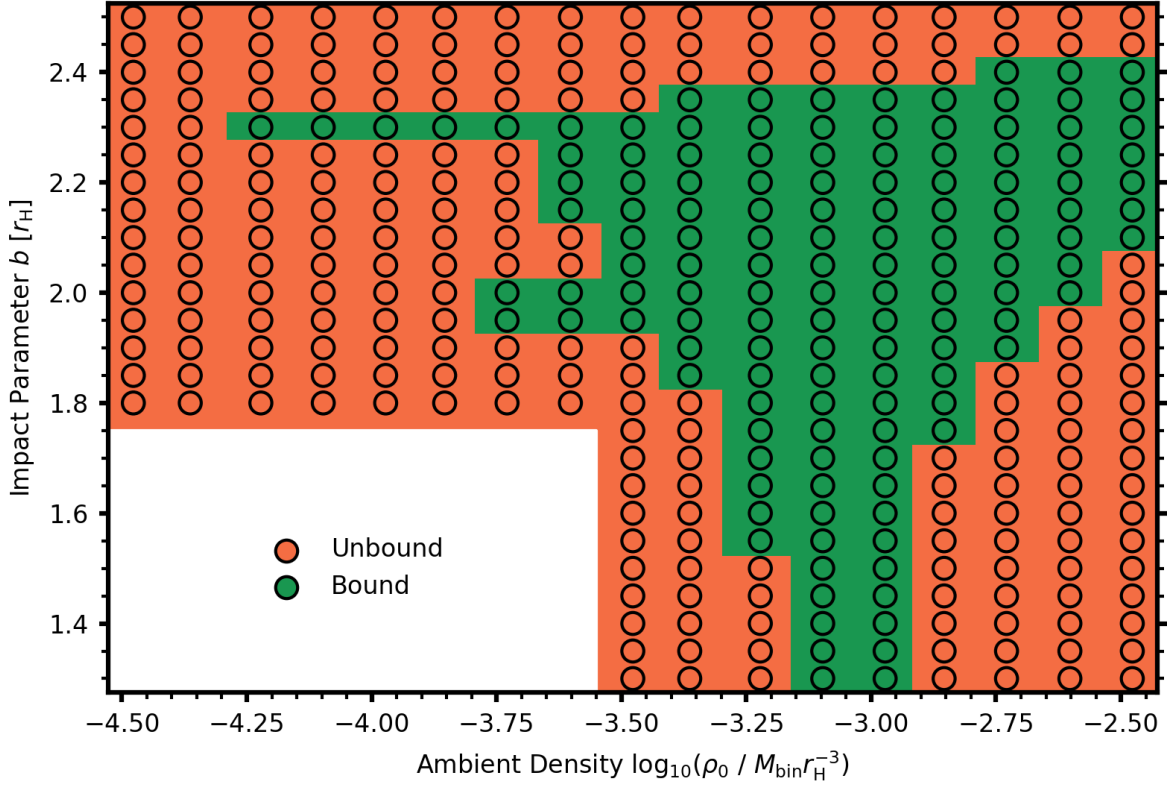
## 5.3 Energetics at First Close Encounter

Figure 11 plots the energy changes during the first encounter between BHs in each of the simulations in the grid. We calculate the energy change during the first encounter by integrating the dissipation from when the BHs first enter their mutual Hill sphere ( $r = r_H$ ). When considering the energetics at periaapsis, we separate effects attributable to the gas and to the SMBH. For gas dissipation, we integrate through to either the first apoapsis, or till the BHs escape the Hill sphere. For SMBH dissipation, we only integrate down to first periaapsis. These ranges allow for the best predictions of energy soon after first close encounter; gas effects are more localised to the periaapsis, whereas the rate of work done by the SMBH weakens as the BH separation decreases within the Hill sphere. We distinguish the data by the depth of first periaapsis  $r_p$  and ambient disc density  $\rho_0$  (by marker size), separating the type of dissipative effect in the 2<sup>nd</sup> and 3<sup>rd</sup> panels. SMBH dissipation is a function of BH trajectory and therefore initial impact parameter, but at high disc densities the gas gravity may be strong enough to perturb the BHs onto different trajectories and so will also have an effect. When considering the relationship between energy dissipated and binary formation outcome, we note that only simulations that dissipate a significant amount of energy during their first close encounter result in successful binary formation, the threshold for this is approximately  $O(E_H)$ . Binaries that do not dissipate enough energy during the first flyby tend to be quickly ionized by the SMBH.

We see that generally, gas gravitation dominates the dissipation but SMBH effects can be significant at lower densities. At first glance, there appears to be little correlation between periaapsis depth and energy dissipated. Finding a clear relationship between SMBH dissipation and periaapsis depth is difficult, as SMBH dissipation is strongly related to the BH trajectory which may change significantly for small perturbations to the initial impact parameter. Furthermore, the relationship between the gas dissipation and periaapsis depth is convoluted by the affect of changing disc density. Focusing only on dissipation by gas, we fit a power law to the energy dissipated during first periaapsis, such that

$$\left| \frac{\Delta E_{\text{gas}}}{E_H} \right| = A \left( \frac{\rho_0}{M_{\text{bin}} r_H^{-3}} \right)^\alpha \left( \frac{r_p}{r_H} \right)^\beta \quad (24)$$

Table 1 lists the best fit parameters, with Figure 12 displaying the results of this fitting, along with the residuals. We exclude the results of high gas density runs with  $\log_{10} \left( \frac{\rho_0}{\rho_*} \right) > -2.8$  runs from the fit due to their significant deviations from the model, suggesting a decoupling at higher densities. The relationship is effectively linear in  $\rho_0$ , i.e.  $\alpha = 1.01 \pm 0.04$ , which we might expect; the mean density and mass of the minidisks prior to the encounter are approximately proportional to  $\rho_0$  and the gas-BH interaction is approximately linear in these quantities, while nonlinear effects such as polarisation and turbulence are apparently subdominant. The simplifying assumptions in the simulation (Eq. 2–4) may lead to this outcome: pressure is sim-



**Figure 10.** Encounter outcomes for BBH with varying initial ambient gas density and initial impact parameter. The 345 simulations are represented by circles, with outcomes colour coded. In the lower density limit, captures are restricted to those impact parameters which result in very deep first encounters with SMBH assist. As density is increased, captures start to occur on a wider range of impact parameters. At very high densities, pre-encounter gas effects induce a drift which reduces the capture cross-section (see Section 5.5)

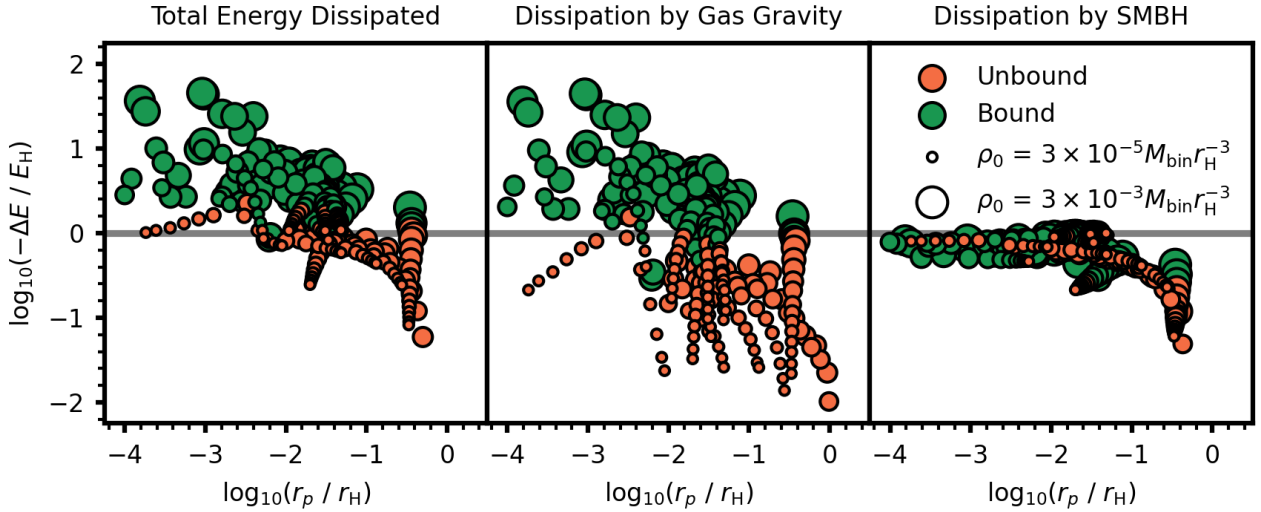


**Figure 11.** Absolute energy changes during the first close encounter separating total energy dissipation, gas gravitational dissipation and SMBH dissipation from left to right. Each simulation is colour coded by its outcome with successful bindings in green and failed in orange. The ambient AGN disc densities  $\rho_0$  are distinguished by marker size, with denser discs given larger markers. SMBH dissipation is bound beneath  $\Delta E \sim E_H$ , whereas gas dissipation ranges from  $10^{-2} - 10^2 E_H$ . Only runs that dissipate enough energy during the first close encounter (around  $1-2 E_H$ ) result in binary formation.

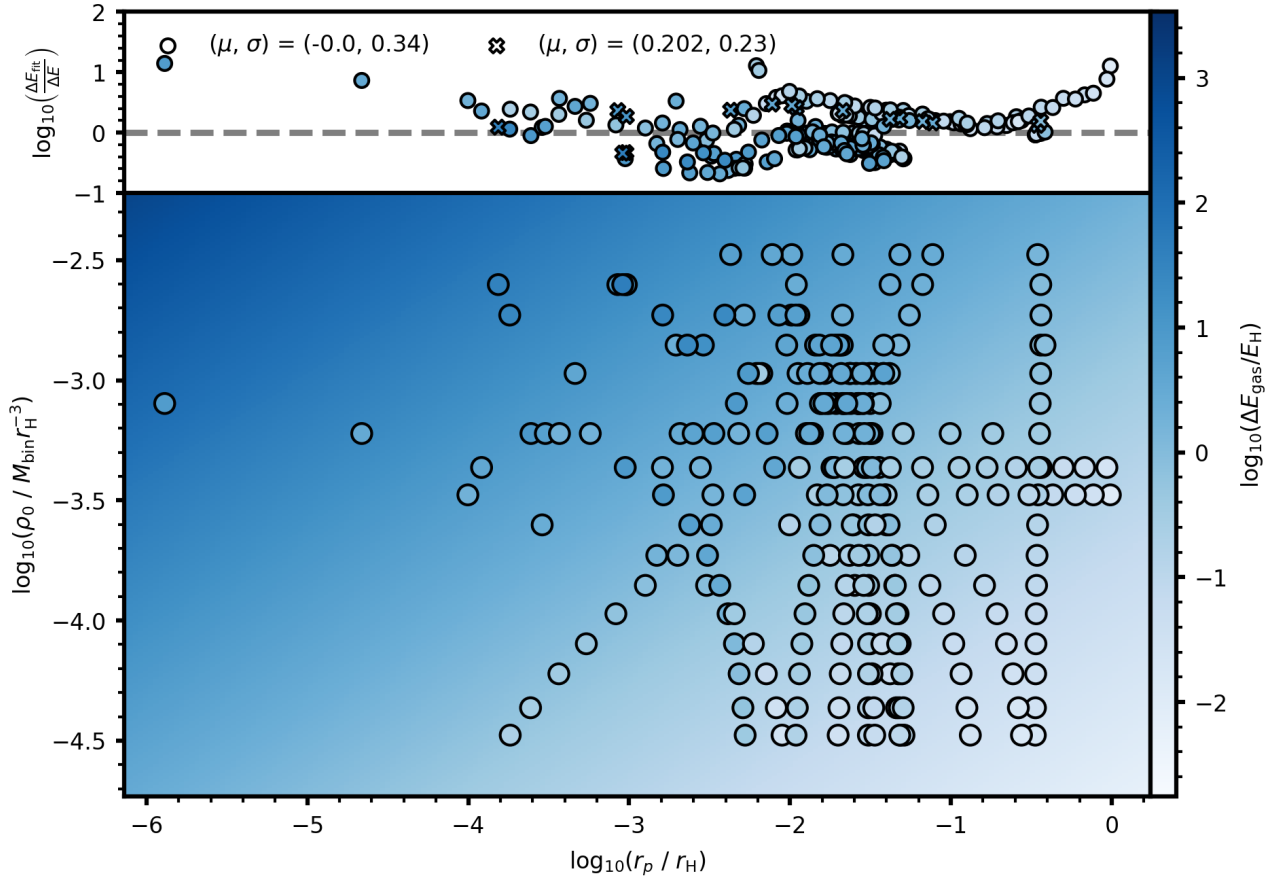


**Figure 12.** Energy changes due to gas dissipation during first encounter, fitted power laws in periapsis depth and ambient disc density (see Eq 24) for all 259 models featuring a close encounter. In the main plot, scatter markers are coloured by the true  $\Delta E_{\text{gas}}$  values recorded by full hydrodynamical simulation. In the background, the mesh is coloured by the predicted  $\Delta E_{\text{gas}}$  associated with that position in  $\rho_0 - r_p$  space. Plotted above are the residuals, comparing the predicted dissipation to the true values. The residuals have an average scatter of 0.3dex, not including those associated with the highest density runs with  $\log_{10}(\frac{\rho_0}{\rho_*}) > -2.8$ , which are excluded from the fit but included in this figure with cross markers to display the overestimation of the gas dissipation at high density.

ply proportional to density, the sound speed and kinematic viscosity are globally fixed and are not allowed to vary in time, and the gas self-gravity is neglected in this study. As discussed in Section 4.4, we expect dissipation to increase for faster, deeper flybys due to the greater disruption of the gas minidisks, though the exact origin of the  $\beta = -0.43$  exponent is harder to identify. Were  $\Delta E$  entirely linear in relative BH velocity, we might expect  $\beta \sim -0.5$  to match the free-fall solution with eccentricity  $e$ ,  $v_p = [GM_{\text{bin}}(1+e)]^{1/2} r_p^{-1/2}$ . On the other hand, faster flybys will naturally feature shorter periods where dissipation is significant, i.e.  $t_p = r_p/v_p \propto r_p^{3/2}$  for nearly parabolic encounters, so it is not immediately clear that faster, shorter flybys should dissipate more energy overall. However, faster flybys are observed to induce more BH-minidisk lag which we expect to be the driving force for differential acceleration across the BH components (as presented in Figure 7). Further more, when comparing relatively shallow encounters, smaller  $r_p$  values will result in the BHs penetrating deeper into the higher density central sections of each other's minidisks, leading to greater gravitational acceleration by gas. Thus we are left with a balance of competing factors that result in a net empirical dependency of  $\Delta E \sim r_p^{-0.43}$ .

There remains a high degree of scatter in the results about the modelled values, and it is clear that periapsis depth and disc den-

sity are not truly independent values (see Figure 13). Moreover, the model regularly overestimates dissipation in the high density limit where  $\log_{10}(\frac{\rho_0}{\rho_*}) > -2.8$ , suggesting perhaps a levelling off in the scaling with density. Regardless, the fit provides a reliable order-of-magnitude estimate for the energy dissipated by gas during the first encounter, a fact we will use in Section 6 for our modelling.

We note here that while we have used  $\rho_0$  to fit our model, it acts only as a proxy for minidisk mass which ultimately dictates the intensity of gas dissipation. If the system were left to evolve for longer before close encounter, the minidisks would attract more gas and grow in mass. We approximate the minidisk mass  $M_d$  as the mass of gas within  $r_H$  of a BH. As all our models evolve for a similar time before close encounter and feature BHs of equal mass we can predict  $M_d$  just before close encounter from the ambient density (specifically, when the two BHs are  $2r_H$  apart).

$$\frac{M_d}{M_{\text{bin}}} \Big|_{r=2r_H} \sim 6 \left( \frac{\rho_0}{M_{\text{bin}} r_H^{-3}} \right) \quad (25)$$

This relationship holds strong for the majority of models in the grid, for the details see Appendix E. However, this relationship is specific to our simulations, it is dictated by our assumptions. Indeed, it is likely that the Hill spheres are not saturated with gas mass and evolving

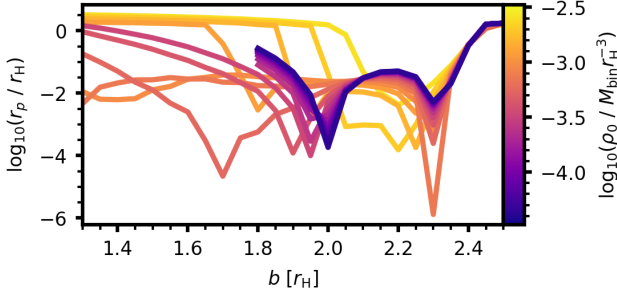


**Figure 13.** Periapsis depth at first close encounter as a function of initial impact parameter  $b$ , and ambient disk density  $\rho_0$ . At low densities the double valley structure matches that of the gas-less trajectories, with maximal angular momentum extracted by the SMBH for  $b \sim 2.0, 2.3r_H$ . As density increases, the inner valley at  $b = 2.0r_H$  starts to move inwards: at intermediate densities the centre of this valley can be found as low as  $b = 1.7r_H$ . The outer valley at  $b = 2.3r_H$  deepens with increasing density, then starts to shift inwards. Past  $\rho_0 \sim 2.5 \times 10^{-3} M_{\text{bin}} r_H^{-3}$ , these trends breakdown and we see a shift towards a single shallow, wide valley structure centered around  $b = 2.2r_H$

the system for longer before the dynamical encounter would allow for more mass accumulation in the minidisks. Nevertheless, using the actual minidisk masses rather than the initial ambient density, the amount of energy dissipation by gas may be estimated more generally.

Curiously, we note that the measured total BH energy dissipation during the first encounter due to gas is consistent with the expression

$$\Delta E_{\text{gas}} = 4.3 M_d v_H v_p \quad (26)$$

where  $v_H = (GM_{\text{bin}}/r_H)^{1/2}$  and  $v_p = (2GM_{\text{bin}}/r_p)^{1/2}$  are the BHs' relative velocity for a parabolic orbit at separations of  $2r_H$  and  $r_p$ , respectively, and  $M_d$  is the mass of a single BH minidisk at BH separations of  $2r_H$  (i.e. Eq. 25 in our simulations). Indeed, Eq. (26) may be written equivalently as

$$\left. \frac{\Delta E_{\text{gas}}}{E_H} \right|_{\text{toy model}} = 293 \frac{\rho_0}{M_{\text{bin}} r_H^{-3}} \left( \frac{r_p}{r_H} \right)^{-0.5} \quad (27)$$

which is reminiscent of Eq. (24) and Table 1. If the fit to the simulations is done by forcing  $\beta = -0.5$  in Eq. (24), then  $A = 295^{+121}_{-86}$  (Eqs. 26–27). Clearly, the dissipation rate calculated from GDF,  $\Delta E_{\text{GDF}} \sim G^2 M_{\text{bin}}^2 \rho_0 v_{\text{BH}}^{-2} r_H = G^3 M_{\text{bin}}^3 \rho_0 v_{\text{BH}}^{-2} v_H^{-2}$  (see also Tagawa et al. 2020; DeLaurentis et al. 2023; Rozner et al. 2023), is inconsistent with the scalings shown by our simulations (cf. Eq. 26). Equation (26) may be useful to build a physical model to explain the measured BH energy dissipation in the simulations. We develop a more accurate predictive model on the outcome of the dynamical encounter in Section (6).

#### 5.4 Asymmetry at Low Gas Density

Knowledge that the binary formation outcome is coupled to periapsis depth helps define the shape of the outcome shape presented in Figure 10, specifically the low density protrusions at  $b \sim 2.0r_H$  and  $2.3r_H$ . As explored in Section 5.1, these impact parameters result in the deepest first encounters in the gas-less limit. This is also the case at low gas densities, as depicted in Figure 13. However, we might question why the tail at  $b = 2.3r_H$  extends to lower densities than the  $b = 2.0r_H$  branch. There is a fundamental difference between

the dynamics in the two valleys: not only does the upper valley ( $b \sim 2.3r_H$ ) have a deep first encounter, but it also has multiple encounters even in the gas-less case. This is because the  $2.3r_H$  valley overlaps with Region B of Boekholt et al. (2023a) where Jacobi captures occur. Conversely, the valley at  $b = 2.0r_H$  does not lie within a Jacobi region: despite the deep first encounter there is no guarantee of a second encounter at low density. While we generally find the first close encounter to be the most significant, we might conclude that the reason why the  $b = 2.0r_H$  valley does not extend to lower densities is because they lack the subsequent close encounters observed in the  $b = 2.3r_H$  valley. The BH trajectories in the  $b = 2.0r_H$  case feature very deep close encounters, but after this the BHs rapidly separate. This might indicate a further dependency within the gas dissipation equation Eq (24), where we should also consider the precise orbital trajectory as well as depth and density. Alternatively, this may be a sampling artefact, with a narrow valley extending deeper at  $b = 2.0r_H$  but beneath our sampling resolution.

We do expect gas capture to be possible within all of the Jacobi encounter regions, as there exist arbitrarily deep encounters in the subsequent close encounters within those regions due to the underlying fractal structure. However, the width of these sub-regions are incredibly narrow and beneath our sampling resolution in  $b$ . The only region obvious in our system is Region B, as it also lies within the valley of deep first close encounter and as such binary formation is easier there. We do observe some members of Region A at small  $b$ , which do not form binaries but do feature multiple encounters (see Section 5.6). There exists also a very narrow Region C for Jacobi encounters at large  $b$ , and while we do observe some looping behaviour around  $b \sim 2.45$ , we do not observe multiple close encounters (where  $r_p < r_H$ ). There presumably exist Jacobi encounters near this  $b$  value which are not sampled by our grid.

#### 5.5 High Density Limit

Many of the rough correlations that hold at low density break down in the high density limit. This is, in part, due to the significant effect gas gravitation can have before close encounter. Within Figure 10, we can identify failed binary formations for  $b \leq 2.05r_H$  at high densities (lower right of panel). These outcomes arise due to self interaction between a BH and its minidisk which result in it being perturbed away from the other BH before a close encounter can occur. By avoiding a close encounter and minidisk collision, the BHs do not undergo significant gas dissipation and so no binary is formed. The rapidity of this migration indicates that this effect is potentially nonphysical. If the BH minidisk is not given sufficient time to stabilise before the BH is allowed to feel the gravity of the gas, irregularities in the disc may lead to a net acceleration not present in the equilibrium minidisk. This effect would likely be suppressed in hotter, more viscous discs as much of the minidisk substructure would be smoothed out sooner. The effect is most pronounced for small impact parameters, as these systems take the longest time to reach close encounter and so the gas has more time to deflect the BHs from their equilibrium trajectories. Future studies may avoid this issue by initialising the BHs in a gas field closer to the steady minidisk state (i.e. improving on the methodology of Appendix C), or preventing the BHs from experiencing gas gravitation feedback until the BHs are within a certain distance.

Conversely, this pre-encounter deflection can actually lead to more binary formation at intermediate densities. Around  $\log_{10} \left( \frac{\rho_0}{\rho_*} \right) \sim -3$  we observe an exceptionally wide area of successful capture. This capture area extends well below the  $b \sim 1.6625r_H$  limit where close

encounters stopped occurring in the gas-less case. Here, close encounters are still able to occur due to the pre-encounter gas-induced drift, which prevents the binary from performing the horseshoe orbits expected at such small radial separations. For a small range of densities near  $\log_{10} \left( \frac{\rho_0}{\rho_*} \right) \sim -3$ , this area of capture extends well beneath the main sampling grid; testing at a coarser  $b$  resolution revealed that horseshoe orbits out-competed the effects of gas drift beneath  $b \sim 0.5r_H$ , resulting in no further close encounters/binary formations. As density is increased beyond  $\log_{10} \left( \frac{\rho_0}{\rho_*} \right) \sim -3$  for small  $b$  values, the strength of the migration is such that close encounters are again prevented, forcing wide flybys.

For systems with densities  $\log_{10} \left( \frac{\rho_0}{\rho_*} \right) > -3$ , almost all binaries that features a mutual Hill sphere intersection result in binary formation. The strength of gas gravitational dissipation can lead to the formation of very hard binaries after only a few periapsis passages. These binaries may be under-resolved by the gas grid, even with AMR, as the binary semi-major axis can approach the local cell size after multiple orbits. At the same time, as the disc gas density increases, we start to enter the regime where the effects of gas self-gravity (which is neglected in this study) may be significant. We can see this in the late time chaotic behaviour of high density systems, where the effect of gas gravitation can strongly perturb the binary orbits on short timescales. For both of these reasons, we do not probe the parameter grid at higher disc densities. Nevertheless, we expect binary formation to be possible, and perhaps even more likely, in the high density regime, but the model in its current state is not designed for such a study.

Many interesting results can still be discerned from the higher density simulations. At large impact parameters, we observe captures without the need for deep close encounters. Figure 14 details the evolution of a run with  $b = 2.4r_H$  and  $\rho_0 = 1.9 \times 10^{-3} M_{\text{bin}} r_H^{-3}$ , where a prolonged dissipation event occurs at a relatively distant separation of  $r_p \sim 0.5r_H$  at  $t = 41$ yr. The resulting binary is soft and retrograde after this first dissipation, but undergoes a more impulsive dissipation event at  $t = 51$ yr during a very close second encounter. During the early binary evolution, the binary is unable to form a cohesive circumbinary disc, maintaining two spiral arms from the initial minidisks. This structure is disrupted by chaotic gas outflows during subsequent hardening periods.

## 5.6 Orbital Direction and Inversion

A different way to visualise the outcome space is to consider the orbital direction of the binary close encounters, and their subsequent angular momentum evolution. Three families of orbits PI, RI, PE (prograde interior, retrograde interior and prograde exterior, see Section 5.1) are expected even in the no-gas system due to the torque exerted by the SMBH. These families are distinct from the 3 regions A, B, C in which Jacobi encounters are predicted (see Figure 9 in Boekholt et al. 2023a). While the families PI, RI and PE are distinguished by the orbital direction at first periapsis, the regions A, B and C are defined by ranges in  $b$  where multiple encounters between unbound BHs are driven by the SMBH. These multiple encounters are Jacobi encounters, and within each Jacobi regions there are further subregions, creating a fractal hierarchy in  $b$ . While these regions were defined originally for the gas-less case, these multiple encounters can still be observed in low-density unbound (and weakly bound) systems.

Figure 15 displays the full outcome grid with extra orbital information. In the low density limit, we identify the transition between

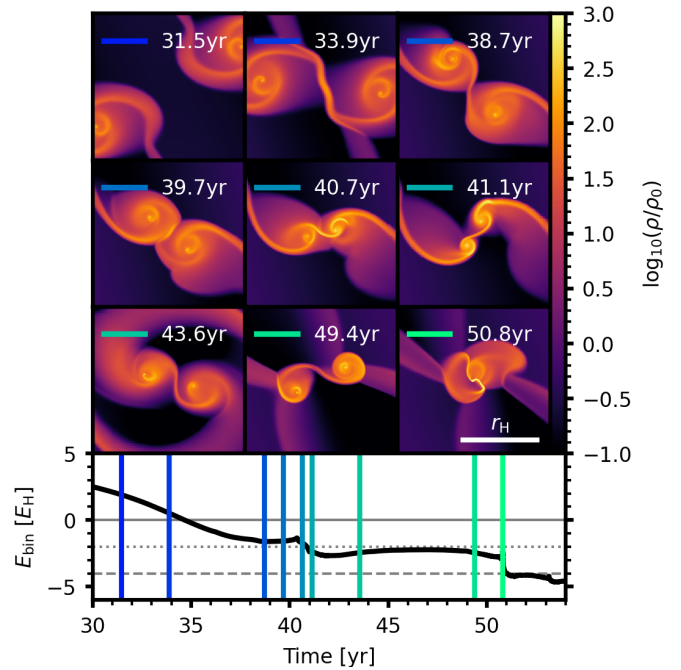


**Figure 14.** Prograde binary formation occurring within dense gas ( $\rho_0 = 1.9 \times 10^{-3} M_{\text{bin}} r_H^{-3}$ ), widely separated ( $b = 2.4r_H$ ) run, displaying the ability for capture to occur without severe close encounters in the presence of significant gas mass. The dissipation period at  $t \sim 41$ yr is more extended than observed in the case of very deep close encounters, but a stable binary is formed regardless.

the orbital families PI, RI and PE: starting at small  $b$  and increasing, we transition from prograde, to retrograde, back to prograde. As density is increased, the gas begins to perturb the BHs from their gas-less trajectories and the positions of these family boundaries shift inwards. The family boundaries represent zero-angular-momentum surfaces, with  $L_{\text{bin}}$  at periapsis ( $L_{\text{bin}}|_{r=r_p} \equiv L(r_p)$ ) changing sign on either side. Because the binary flybys are approximately parabolic, systems near this surface also have the deepest first close encounters. Of the 133 binaries that form, 99 are initially retrograde (74%). These binaries all form during retrograde interior (RI) encounters on intermediary impact parameters, representing the majority of formed binaries. In the high density limit however, we observe preferential prograde binary formation which may extend beyond our parameter grid.

Orbital inversion occurs when the binary angular momentum changes sign, resulting in a flip from prograde to retrograde or vice versa. In principle this can be induced either by gas gravitation torques or by the SMBH but in our systems the latter tends to dominate. We inspect the grid for the presence of orbit reversal in the post-first-encounter evolution, which we identify by the existence of a later periapsis encounter within the Hill sphere with inverted angular momentum to the initial periapsis. Systems that experience an orbital inversion are marked as a “flip” in Figure 15.

Inversions are observed in both bound and unbound systems. For an unbound system to experience an inversion, they necessarily require a second close encounter. As such the unbound inversions that we record in Figure 15 are a sign that we are observing Jacobi encounters. The large number of unbound inversions observed at low density between  $b = 2.05 - 2.3r_H$  are Jacobi encounters from Region B, made more easily visible as the light green region of Figure G where

systems are distinguished by their number of encounters. We also identify a few encounters from Region A near  $b \sim 1.8r_H$ , though only one of these experiences an inversion.

Orbital inversion can also occur in bound systems. These inversions come in two types: Jacobi-like inversions and zero-angular-momentum inversions. In the former case, gas dissipation is significant enough to drive binary formation, but the young binary is still wide enough for the SMBH to drive the same inversion observed in the unbound case. These systems are observable in Figure 15 at  $\log_{10} \left( \frac{\rho}{\rho^*} \right) \sim -3.6$  between  $b \sim 2.05 - 2.25r_H$ . They only perform a single inversion during their first period, such that the resulting stable binary is prograde despite the initial retrograde encounter. Orbital inversion is also possible near the zero-angular-momentum surfaces. Binaries formed near this surface have a very small absolute angular momentum after the first periapsis, and so very little torque is required to force them through an inversion. This is why even at higher densities, we see flips occurring near the prograde-retrograde boundaries.

Even in systems bound by gas dissipation, the actual inversion is consistently driven by SMBH torques. These torques are strongest when the binary is wide and soft, so we generally observe inversion within the first binary period, before significant hardening can occur. This helps explain why we do not observe any inversions within the central capture region away from the zero-angular-momentum surfaces: these systems have relatively large absolute angular momentum, and are too hard for the SMBH torque to be strong enough to drive inversion. It should be noted that the Jacobi-like inversions and zero-angular-momentum inversions are not totally distinct, the upper zero-angular-momentum surface at  $b \sim 2.3r_H$  overlaps with Region B of the Jacobi encounters.

## 5.7 Gravitational Wave Dissipation

It is expected that if the formed binary hardens over time the BHs will eventually be close enough for GW dissipation to be significant. While we do not evolve our formed binaries for a long time after capture, we might still consider the comparative power of gas hardening to hardening by GW emission during the first close encounter. The two processes share a general chronology for elliptical binaries: strong dissipation at periapsis followed by quiescence when the two bodies are distant. General relativistic effects are not included within the simulation (in a post-Newtonian form or otherwise), but we can still make predictions for the energetic contributions of GWs were they included. We can compute the energy lost at periapsis by Peters (1964).

$$\Delta E_{\text{GW}} = -\frac{\pi}{120} \frac{G^{\frac{7}{2}}}{c^5} \frac{M_{\text{bin}}^{9/2}}{r_p^{\frac{7}{2}}} g(e) \quad (28)$$

$$g(e) = 96 + 292e^2 + 37e^4. \quad (29)$$

To get GW dissipation of a magnitude significant enough to affect the binary motion, we invert Equation (28) to find the periapsis required for  $\Delta E_{\text{GW}} \sim 0.1E_H$ , in the extreme case that  $e \sim 1$ . We find that, this requires a periapsis depth less than  $r_p \sim 5(Gc^{-2}M_{\text{bin}}/r_H)^{5/7}r_H \sim 10^{-5}r_H$ . Of all simulations, we only find a single run with this depth at first close encounter,  $(b, \rho_0) = (2.3r_H, 7.9 \times 10^{-4}M_{\text{bin}}r_H^{-3})$ , which has an initial periapsis depth of  $r_p \sim 10^{-6}r_H$ . In this case, the periapsis is deep enough that a binary would form by GW dissipation without need for gas effects. However, as binary formation was already predicted by gas effects for this model, the non-inclusion of post-Newtonian physics has no qualitative effect on the outcome.

For our equal mass system and considering the limit  $e \sim 1$ , we can consider the boundary periapsis depth at which the energies dissipated by GW exceed that by gas dissipation (combining Eq. 28 and Eq. 24)

$$\left( \frac{r_p}{r_H} \right)^{\beta+\frac{7}{2}} < \frac{85\pi}{24A} \frac{G^{\frac{7}{2}}}{c^5} M_{\text{bin}}^{\frac{9}{2}} r_H^{-\frac{7}{2}} \left( \frac{\rho_0}{M_{\text{bin}}r_H^{-3}} \right)^{-\alpha} \quad (30)$$

For any specified SMBH-BH-BH configuration, we can predict the threshold beneath which we expect GW dissipation to dominate over gas dissipation. Within our system, this reduces to

$$\frac{r_p}{r_H} \lesssim 10^{-10} \left( \frac{\rho_0}{M_{\text{bin}}r_H^{-3}} \right)^{-0.33} \quad (31)$$

The prefactor  $10^{-10}$  indicates that gas dissipation will remain dominant over GW dissipation for all but the deepest of close encounters or incredibly low density systems. In performing this calculation we have been forced to make a likely flawed assumption, asserting that the fitting procedure introduced in Section 5.3 will extrapolate down to exceptionally deep close encounters. We have only a few runs with a first periapsis beneath  $\sim 10^{-4}r_H$ , and we might expect that for very deep encounters the dependency of gas dissipation on depth may level off. If this is true, then GW dissipation may become more important for slightly shallower encounters. Regardless, we expect such extremely deep encounters to represent a very small proportion of the total encounters, so it remains fair to conclude that for the vast majority of encounters gas dissipation will be the dominant mechanism for binary formation.

## 6 PREDICTIVE MODELS

The simulations presented above represent a large dataset of failed and successful binary formations. From this dataset, we attempt to construct an empirical predictive model that may allow one to obtain the outcome of the encounter without having to simulate the entire encounter. This is intended to improve on the currently used models (Goldreich et al. 2002; Tagawa et al. 2020; DeLaurentiis et al. 2023; Rozner et al. 2023), which typically rely on adjustments of the Ostriker (1999) gaseous dynamical friction formula valid in an infinite homogeneous medium and contradict the inferred energy dissipation rate in our simulations (Eq. 26). In order to do this, we use the dynamic properties of the binary at Hill sphere intersection to predict the conditions at periapsis. As discussed in Section 5.3, if the periapsis depth and ambient disk density are known, a reasonable estimation can be made for the energy dissipated by gas. We apply this modelling to the 259 models featuring a ‘‘close encounter’’ where the BHs approach within  $r = r_H$ , as otherwise capture failure is assured.<sup>4</sup>

### 6.1 Predicting Periapsis Quantities

Each of the first encounters are approximately parabolic at periapsis; this approximation is strongest for  $r_p \ll r_H$ . As such, we have analytical means to calculate the periapsis depth provided the specific

<sup>4</sup> We also exclude the run with the very high gas mass  $(\rho_0, b) = (3.3 \times 10^{-3}M_{\text{bin}}r_H^{-3}, 2.05r_H)$  despite technically reaching  $r = r_H$ , as it features a very shallow turn-around trajectory that does not obey the general trends

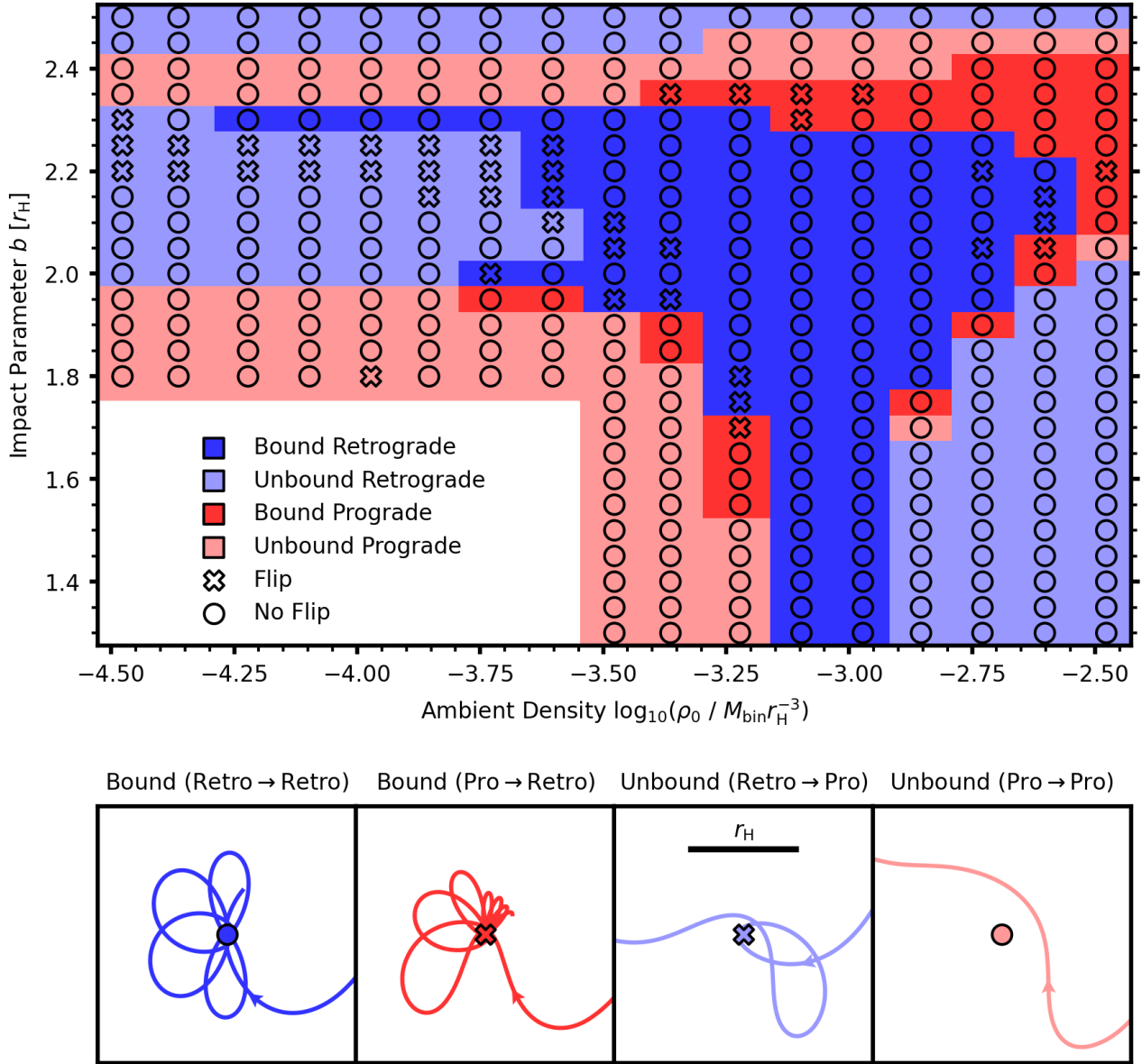


**Figure 15.** Outcome grid as in Figure 10, but with sub-regions to better distinguish class of first close encounter (retrograde or prograde). For each simulation, marker type indicates the existence of orbit reversal in the post-encounter system. Multiple clear borders are found between prograde/retrograde encounters, along which orbit reversals may occur. Orbit reversal is also possible for the marginally bound retrograde systems near  $\log_{10}\left(\frac{\rho_0}{\rho_*}\right) \sim -3.5$ , where the SMBH torque remains significant post binary formation. The lower panel exhibits example encounters from the grid, with the trajectory of the outer BH traced in a frame centred on the inner BH.

angular momentum at periapsis  $L(r_p)$  is known:

$$r_p = \frac{L(r_p)^2}{2GM_{\text{bin}}\mu^2} \quad (32)$$

We find that this relation holds approximately for all but the shallowest of first encounters (where  $r_p \sim r_H$ ). The question then becomes how best to calculate the periapsis angular momenta. In the 3 body SMBH-BH-BH system,  $L_{\text{bin}}$  is not conserved and the torque exerted by the SMBH will depend on the BH trajectories. In comparing the binary angular momentum at Hill intersection ( $L_{\text{bin}}|_{r=r_H} \equiv L(r_H)$ ) and at periapsis, we find a twin forked solution. Figure 17 displays these two families of solutions and exhibits the separating factor: the

entry angle into the Hill sphere  $\theta$ . Figure 16 describes the geometry of  $\theta$ : the angle between the  $x$  (or  $R$ ) axis and the BH-BH separation upon first Hill sphere intersection. The amount of angular momentum exchanged between the binary and the SMBH varies depending on whether the outer BH leads or trails the inner BH on Hill intersection. As such, two branches of solutions form depending on the entry angle  $\theta$ . The trend is consistently linear outside of a complicated interaction area around  $\theta \sim 0$ ; here the absolute angular momentum is large and so there is less need for a quality fit. In attempt to fit these branches, we apply 3 linear fits dependent on  $L(r_H)$  and  $\theta$ , in the form  $y = mx + c$ , where  $m$  and  $c$  are specified in the legend in Figure 17.



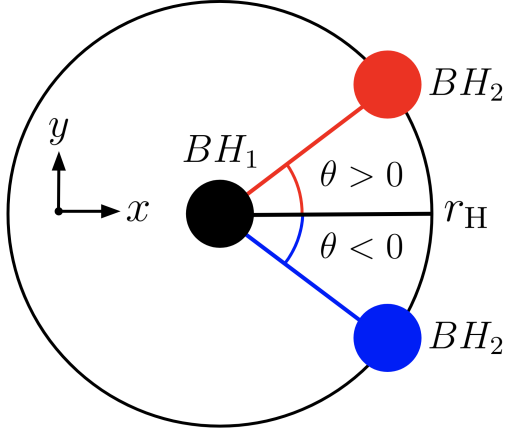


**Figure 16.** Diagram for the definition of the entry angle  $\theta$ . We measure  $\theta$  when the two BHs first penetrate their mutual Hill sphere, between the SMBH radial direction (in the shearing frame  $x$  direction) and the BH-BH separation vector. The angle is measured in the frame of the BH originating on the inner orbit.

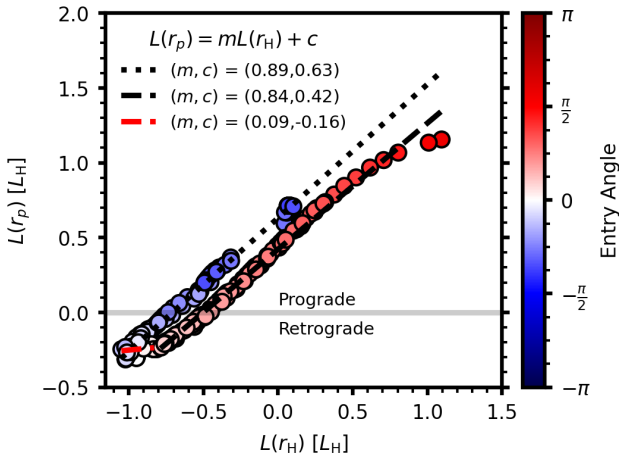


**Figure 17.** Twin forked structure in angular momentum space, when comparing angular momentum at Hill intersection  $L(r_H)$ , to angular momentum at periastris  $L(r_p)$ . Membership to the two branches depends on the BH trajectory. If the outer BH leads the inner BH on Hill intersection, less angular momentum is injected. If the outer BH trails the inner BH on intersection, more angular momentum is injected. Within each family, a strong linear relationship is present, though this becomes more complicated near  $\theta \sim 0$ . The legend details fitting values for the 3 linear branches of form  $y = mx + c$ .

Angular momentum fitting is applied by first distinguishing the upper and lower angular momentum branches, and removing the elbow section at large negative  $L(r_H)$ . Any system with  $\theta < 0$  necessarily belongs to the upper branch, and is used to fit the black dotted line. For systems with  $\theta > 0$ , we apply a cutoff at  $L(r_H) = -0.8L_H$  due to the gradient change identified here. Systems with more negative angular momentum provide the fit for the red dashed line, the rest the black dashed line. When predicting  $L(r_p)$  for a new system, we first identify which branch it should belong to, then use the corresponding linear fit to identify its periastris angular momentum.

**Table 2.** Best fit parameter values and dispersion ( $\sigma$ ) for the complete predictive modelling framework.

variable	value	$\sigma$
$\log_{10}(A)$	2.63	0.17
$\alpha$	1.01	0.04
$\beta$	-0.43	0.03
$B$	-1.43	0.02
$C$	0.47	0.02

With these two fits in hand, we can attempt to predict  $r_p$  as a function of  $L(r_H)$  and  $\theta$ . We find that the fit performs well for large  $r_p$ , but poorly for very deep encounters. This is not surprising, here small absolute changes in  $L(r_p)$  can result in large changes in  $r_p$  in log space. See Appendix F for a full breakdown of fitting errors. Propagating these values through, we now use the predicted  $r_p$  values with the ambient gas density  $\rho_0$  to calculate the energy dissipated by gas using Equation (24). As shown in the bottom right panel of Figure F, the majority of predicted values fall within 0.4dex of the real values. The main contributors of error are due to miscalculations of periastris depth for low-angular-momentum trajectories, and the relative large uncertainties generated from fitting Equation (24).

With a reasonable predictor for  $\Delta E_{\text{gas}}$  formed, we now consider the energy dissipated by the SMBH. This proves to be a simple relation tied directly to the entry angle  $\theta$ , or more specifically the radial projection of BH separation at Hill sphere encounter  $\cos(\theta)$  (see Figure 18). This fit has very little spread from the true value, despite some unknown multi-valued relationship at large negative  $\theta$ . SMBH dissipation is maximised when both of the BHs and the SMBH are in conjunction (small absolute  $\theta$ ): here the SMBH tidal force acts directly against the BH relative velocity. For the more azimuthal aligned interactions (large absolute  $\theta$ ), the SMBH tides are less aligned with velocity and so SMBH dissipation is lessened.

We can now predict the binary energy immediately after the first periastris passage as

$$E_{\text{bin,post}}(r_p, \theta, \rho_0) = E_{\text{bin}}|_{r=r_H} + \Delta E_{\text{gas}}(r_p, \rho_0) + \Delta E_{\text{SMBH}}(\theta) \quad (33)$$

where  $E_{\text{bin}}|_{r=r_H}$  is the initial energy of the BHs at Hill intersection,  $\Delta E_{\text{gas}}(r_p, \rho_0)$  is given by Equation (24) repeated here for convenience and  $\Delta E_{\text{SMBH}}(\theta)$  is the fit

$$\frac{\Delta E_{\text{gas}}}{E_H} = A \left( \frac{\rho_0}{M_{\text{bin}} r_H^{-3}} \right)^{\alpha} \left( \frac{r_p}{r_H} \right)^{\beta} \quad (34)$$

$$\frac{\Delta E_{\text{SMBH}}}{E_H} = B \cos(\theta) + C \quad (35)$$

where  $(A, \alpha, \beta, B, C)$  are fitting constants given by Table 2 and a periastris depth  $r_p$  predicted by the parabolic approximation

$$r_p = \frac{L(r_p)^2}{2GM_{\text{bin}}\mu^2} \quad (36)$$

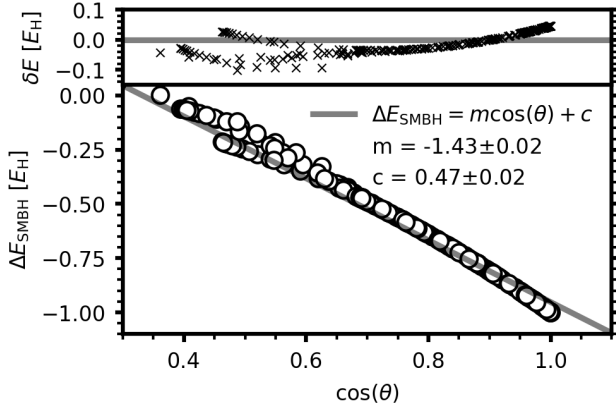
for a given periastris angular momentum  $L(r_p)$  predicted by  $\theta$  and  $L(r_H)$  the binary entry angle and angular momentum at Hill intersection

$$\frac{L(r_p)}{L_H} = m \frac{L(r_H)}{L_H} + c \quad (37)$$

$E_{\text{bin,post}}$  acts as an predictive estimator of the expected binary energy immediately after the first periastris. A complete breakdown of the errors introduced by each fitting step can be found in Appendix F. We use this energy estimator to predict the hardness of the binary and determine whether or not we expect the binary to remain bound.

**Table 3.** Best fit parameter values for angular momentum propagation from Hill sphere penetration to periapsis (see Equation (37))

m	c	case
$0.89 \pm 0.008$	$0.63 \pm 0.006$	$\theta < 0$
$0.84 \pm 0.008$	$0.42 \pm 0.004$	$\theta \geq 0$ and $L(r_H) > -0.8L_H$
$0.09 \pm 0.098$	$-0.16 \pm 0.083$	$\theta \geq 0$ and $L(r_H) \leq -0.8L_H$

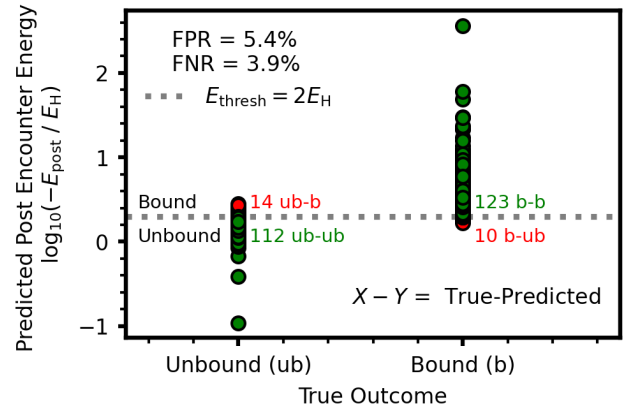
**Figure 18.** Correlation between entry angle  $\theta$  with  $\Delta E_{\text{SMBH}}$ , the energy removed from the binary by the SMBH for all 259 simulations featuring mutual Hill sphere intersections. See Figure 16 for details of the entry angle geometry. The relationship is well fit linearly in  $\cos(\theta)$ , though the residuals appears to be double valued at small  $\cos(\theta)$  suggesting the dependence of  $\Delta E_{\text{SMBH}}$  on some second unidentified parameter. We do not attempt to identify this parameter, as the fit remains of reasonably high quality regardless

### Summary of Predictive Binary Capture Model

- Step I Identify system properties at Hill intersection: binary energy, angular momentum, entry angle and ambient density
- Step II Predict angular momentum at periapsis by the twin-fork fitting with Eq (37) and Table 3
- Step III Predict periapsis depth with the angular momentum at periapsis and Eq (32)
- Step IV Predict dissipation by gas via periapsis depth and ambient density with Eq (34) and Table 2
- Step V Predict dissipation by the SMBH via the entry angle with Eq (35) and Table 2
- Step VI Calculate the post-encounter energy  $E_{\text{bin,post}}$  by Eq (33)
- Step VII If  $E_{\text{bin,post}} < 2E_H$ , the binary is predicted to be bound after the first close encounter

## 6.2 Testing the predictive model

In determining the outcome of a close encounter we apply the same stability criterion introduced in Section 4.3: any binary which achieves  $E_{\text{bin}} < 2E_H$  we expect to remain bound. We now use our predicted energies  $E_{\text{bin,post}}$  to assess what close encounters we expect to result in successful binary formation. Of the 345 models in the simulation grid, 259 feature a mutual Hill sphere intersection: the re-

**Figure 19.** Accuracy of predictive modelling for the 259 simulations that feature a close BH-BH interaction. Prediction sets are labelled in format  $X - Y$  where  $X$  is the true outcome and  $Y$  is the predicted outcome. While the predicted dissipated energy is sometimes very different from the true dissipation, the model succeeds in predicting the outcome the vast majority of the time: 91% of models have the same predicted and "true" outcome. The false positive and false negative rates (FPR and FNR respectively) are only 5.4% and 3.9%.

maining 86 models are marked as unbound necessarily. We apply our predictive modelling to the 259 intersecting models, finding that our predictions match the true simulation outcome for 91% of cases, as displayed in Figure 19. Figure 20 indicates that location of false positive and negatives, identifying that failed predictions are most likely on the fringe of the capture region identified in Figure 10. We find our model is able to correctly predict the outcome of a flyby event for the vast majority of the simulations, despite the considerable scatter in exact predicted energy. This methodology may prove to be useful when coupled with global AGN simulations that attempt to predict BBH formation/merger rates without including a full hydrodynamical treatment, such as in Secunda et al. (2019) or Tagawa et al. (2020) which originally used simplified prescriptions for this process which are inconsistent with our numerical simulations. While our system only considers a subset of possible interaction types (no initial inclination, eccentricity), this is a step forward for semi-analytical models. We summarise each step of the predictive model below:

## 7 DISCUSSION

### 7.1 Comparison to Literature

There have been many recent papers that address the formation of BBHs in AGN discs. Their methodologies vary in terms of simulation type, domain, initial conditions and simulated physics. In adopting initial conditions similar to that of CR1 we attempt to provide a clear comparison for gas-assisted BBH formation between SPH and a static Eulerian grid code (PHANTOM and Athena++). We explore a different density space to that of CR1; our most dense model is comparable to their low disk mass system. As well as this, they also included accretion in their study, which we neglect, finding it to be the dominant driving force of binary dissipation during close encounters. Despite this, we report the same dissipation chronology: BHs form their own gaseous minidisks which then collide during close encounters, dissipating orbital energy by gas gravitation. In

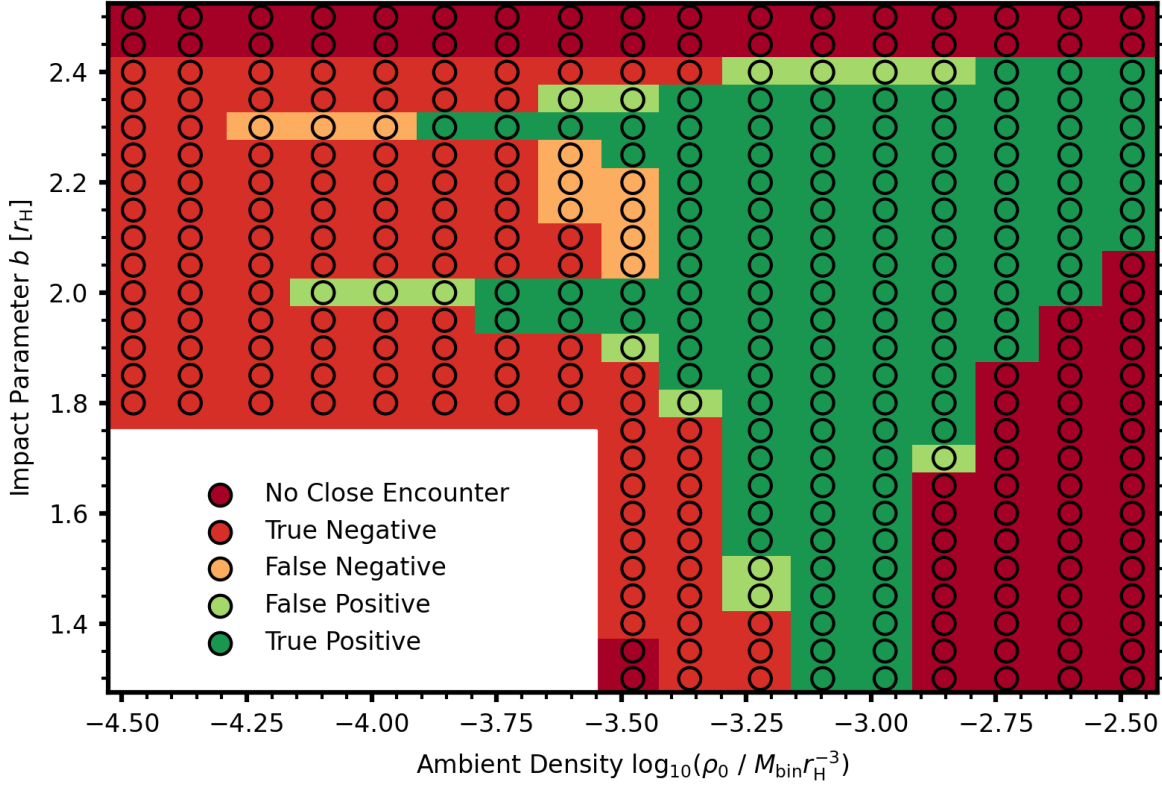


**Figure 20.** Predictor accuracy in the  $b - \rho_0$  outcome space. Inaccurate predictions are located entirely on the fringe of successful binary formation, with the majority of the capture space well predicted. The model only makes incorrect predictions along the boundary between successful and unsuccessful capture, notably struggling to correctly predict binary formation for the very deep close encounters associated with  $b = 2.0, 2.3r_H$ . 86 models feature no close encounter and so necessarily do not form binaries (show here in dark red).

both studies, binaries form successfully during only a single close encounter.

Li et al. (2023) analyses a similar capture scenario to our own, studying an annulus of the AGN gas disc using the 2D hydrodynamical grid code LA-COMPASS. They study a thicker, hotter disk with  $H/R \sim 0.01$ , and vary azimuthal BH-BH separation instead of radial, but they still observe BBH formation by gas gravitational dissipation alone, without the need for accretion. They also put forward a predictive model for binary formation based on BBH energy at  $r = 0.3r_H$  and local disc gas mass. We do not find significant agreement with this model, as we predict periapsis depth to be as, if not more, important than incident energy. However, as with CR1, Li et al. (2023) considers a more massive gas density than our own study, equivalent to (and exceeding) our most massive models. They only form retrograde BBHs, likely due to their selection of a single radial separation.

Recent semi-analytical studies (Tagawa et al. 2020; DeLaurentiis et al. 2023; Li et al. 2022; Rozner et al. 2023) examined embedded binary formation by means of Ostriker (1999) gas dynamical friction (GDF). We do not find GDF to be an accurate description of the drag observed in our system, where the geometry of the gas distribution is especially important and so the assumption of a homogeneous gas background is inappropriate. Furthermore, we find that deeper and faster encounters dissipate more energy proportional to  $v_p$  as (Eq. 26) as opposed to in GDF where drag scales as  $v_p^{-2}$  with velocity (for supersonic trajectories). Despite this, these studies predict stable, eccentric BBH formations similar those observed in our hydrodynamic

simulations. In particular, Figure 9 of DeLaurentiis et al. (2023) provides a similar  $b - \rho_0$  cross section to our own Figure 10, displaying a similar extension of captures to smaller impact parameters as density increases as in our results, but that paper did not find captures at large  $b$  when density is high. However, our simulations assumed initially corotating BHs with the AGN disc. It is possible that in systems with nonzero initial BH eccentricity or inclination, where each BH has a large relative velocity to the ambient gas, the formation of minidisks would be suppressed. In this case, GDF may prove a more reliable prescription, but that case is beyond the scope of this paper.

The closest comparison can be made between this study and the companion study CR2, as it also considers interactions over a range of initial separations and two different densities, albeit with a different numerical method, the smoothed particle hydrodynamics (SPH) code PHANTOM. The results are in broad agreement: we find encounters over a similar range of impact parameters, within the valley defined by encounters with the deepest periapsis. In both studies, the fractal flyby structure reported in the gas-less case by Boekholt et al. (2023a) is not observed, which is likely due to the relatively low resolution in the  $b$  space. The binaries in this paper lose similar amounts of energy by gas dissipation during close encounters as in CR2, generally on the scale of 1-10  $E_H$ . Most importantly, we observe very similar dependencies of gas dissipation on periapsis depth, where  $\Delta E_{\text{gas}} \propto r_p^\beta$ . In this work, we recovered  $\beta = -0.43 \pm 0.03$  (Eq. 24 and Table 24), pleasingly similar to the  $\beta = -0.42 \pm 0.16$  derived in CR2 though the latter features a considerably wider spread, perhaps influenced by the lower number of models available to fit with. The

ability of studies with fundamentally different simulation methodologies (Eulerian AMR vs SPH) to reproduce this exponent shows promising indications that this is may be a intrinsic property of gas dissipation. It should be noted that the two studies are not in total agreement, CR2 implemented normalised initial azimuthal separations that kept the time to encounter between runs consistent. This likely explains why CR2 continues to observe a very wide capture window at high density, at which point this study recorded a reduction in cross section due to migratory effects (see Section 5.5). Moreover, CR2 implements a different predictive methodology for binary outcome, where dissipation by SMBH and gas effects are calculated together instead of separated.

There appears to be general agreement with both analytical and hydrodynamical models that close encounters between BHs in AGN discs should lead to the formation of highly eccentric, stable BBHs. We believe our wider parameter space, with fully hydrodynamical implementation, offers the best coverage of possible formation encounters presented in the literature so far.

## 7.2 Limitations and Caveats

In our simulations we adopt several assumptions that should be considered when interpreting the results and may warrant further study:

- *BH Feedback*: we have neglected any feedback from the BH into the AGN disc by jets or winds. Future studies may want to include a sub-grid prescription to account for these effects, even if the near-BH effects are not fully resolved.
- *Gas Self Gravity*: we have neglected gas self-gravity due to the increased computational expenditure required for such simulations. While this is a good approximation for the low ambient density models, as we increase the disc density this assumption weakens. Studies into higher disc masses should be careful in considering gas self-gravity as its inclusion will likely change gas morphology and subsequently the binary evolution.
- *Thermodynamics*: we have adopted an isothermal equation of state to simplify our system. In real AGN systems we expect contributions to the fluid energy and pressure from radiation, as well as heating and cooling effects. The competition between between viscous dissipation, shock heating and radiative cooling is likely to lead to variations in pressure throughout the gas, which may change minidisc viscosities and densities and subsequently the capture likelihood.
- *Non-coplanar Interactions*: by restricting ourselves to a 2D simulation, we have considered only interactions that occur in the plane of the disc. We expect BHs in AGN to exist in orbits of varying inclinations, and previous studies have suggested that these inclinations should have a strong effect on capture/close encounter probability (Samsing et al. 2022).
- *Eccentricity*: we launch our black holes on Keplerian trajectories in the shearing box, simulating circular orbits in the AGN disc. Introducing eccentricity to the initial conditions will likely change the nature/probability of close encounters and non-zero BH velocity relative to the ambient gas may effect the ability for BHs to form stable mini-discs before encounter.
- *Shearing Box*: we have simulated only a patch of a globally varying disc. In doing so we have massively reduced the computational expense, but are unable to consider the global effects such as potential gap clearing by the BHs. While our findings are consistent with CR2 which simulated a global disc annulus, this simplification may become more important as more massive interacting BHs are considered.
- *Predictive Modelling*: while our predictive model accurately de-

scribes our own systems, the strong connections between Hill quantities and periapsis quantities may break down when considering a wider spread of initial conditions e.g. BH eccentricity and inclination.

- *Unresolved shocks*: despite use of AMR to finely resolve the gas morphology near the BH, we still experience some numerical difficulties in properly resolving the shock structure during close encounter. A more detailed discussion of the difficulties presented and solution adopted can be found in Appendix D.
- *Synchronisation*: the nature of the shearing box means models with smaller impact parameters take longer to reach close encounter. This means that they have longer to accumulate minidisc gas, a disparity between models. It can also lead to deflection from the equilibrium trajectories long before close encounter, which can either prevent or encourage close encounters. This study could be improved by offsetting the BH azimuthal separations to ensure similar encounter times for different impact parameters (such as implemented in CR2), although the agreement between the two studies suggest that the results are not sensitive to this assumption.

## 8 SUMMARY AND CONCLUSIONS

In this study we simulated 345 flyby interactions between two isolated BHs on co-planar circular orbits in an AGN disc by spanning a parameter space in disc density and interactor impact parameter. We identified a region of feasibility where binary capture is expected to occur, accounting for 133 of the 259 systems featuring a close encounter. We introduced a predictive modelling framework for binary formation based on binary conditions at Hill sphere intersection. We summarise the key findings below:

- Dissipation by gas gravitation is sufficient to form stable binaries from isolated black holes in AGN discs. Upon approach, each BH perturbs the other's gaseous minidisc. When the discs collide, much of the minidisc gas is forced to trail behind the binary components, resulting in drag and dissipation of orbital energy. For close encounters, this dissipation occurs rapidly over a short period localised to the periapsis. Extended dissipation may also drive formation for wider encounters in more gas dense systems. We do not find the dissipative dynamics to be in good agreement with the gas dynamical friction prescriptions often applied to these systems.
- We identify an extensive region in the impact parameter - initial ambient density ( $b - \rho_0$ ) space where binary capture is efficient (Figure 10). At low density, successful captures are restricted only to  $b$  values where the close encounters are very deep, but the region widens as density increases.
- Capture likelihood is strongly tied to depth of first periapsis and only binaries that dissipate a significant proportion of their energy ( $\Delta E \sim 2E_h$ ) during the first encounter form stable binaries. We find that the magnitude of energy dissipation by gas is well fit by power laws in periapsis depth and initial disc density such that

$$\Delta E_{\text{gas}} \propto \rho_0^{1.01 \pm 0.04} r_p^{-0.43 \pm 0.03} \quad (38)$$

This fit weakens at higher initial ambient densities, overestimating dissipation above  $\rho_0 \sim 2.5 \times 10^{-3} M_{\text{bin}} r_{\text{H}}^{-3}$ .

- The measured dissipation of BH energy by gas is also roughly consistent with the simple expression

$$\Delta E_{\text{gas}} = 4.3 M_{\text{d}} v_{\text{H}} v_{\text{p}}, \quad (39)$$

where  $v_{\text{H}} = (GM_{\text{bin}}/r_{\text{H}})^{1/2}$  and  $v_{\text{p}} = (2GM_{\text{bin}}/r_{\text{p}})^{1/2}$  are the BHs' relative velocity for a parabolic orbit at separations of  $2r_{\text{H}}$  and  $r_{\text{p}}$ ,

respectively, and  $M_d$  is the mass of a minidisc at BH separations of  $2r_H$ .

- Gas assisted capture is possible even for very low initial ambient gas densities or minidisc mass, provided the initial impact parameter lies within the narrow valleys resulting in very close encounters (near the zero-angular momentum trajectories). In these encounters, the very high relative BH velocity as well as the strong disruption of each BH minidisc drives strong dissipation.
- The binaries formed can be retrograde or prograde with respect to the AGN disc; while the former is more likely at lower densities, at higher densities the latter dominates (Figure 15).
- Formed binaries tend to be highly eccentric ( $e > 0.8$ ), we do not observe a general trend towards circularisation during the first  $O(10)$  binary periods. The angular momentum evolution post formation depends on the hardness of the binary, SMBH effects tend to dominate unless the binary is very hard. Stable binaries may undergo orbital inversion due to SMBH effects within the first few periods.
- The predicted dissipation by GW emission remains sub-dominant to gas dissipation for the vast majority of runs. We expect GW dissipation to dominate only for exceptionally deep close encounters at very low gas density. Gas effects dominate binary formation for a much wider range of impact parameters.
- We provide accurate predictions as to the outcome of a binary formation event based only on quantities measurable at Hill sphere intersection (Section 6). For our system, these predictions match the hydrodynamically derived outcome 91% of the time (Figure 20). This modelling framework will be beneficial to semi-analytical studies by providing an inexpensive predictive methodology that is in strong agreement with the full hydrodynamical simulations while only using quantities available to  $N$ -body codes.

In simulating the hydrodynamics and  $N$ -body dynamics of the interaction between BHs in a gaseous disc, we affirm the ability for gas gravitation to encourage the formation of BBH in AGN discs and conduct a thorough analysis of the underlying physics processes.

## ACKNOWLEDGEMENTS

All simulations presented in this paper were performed on the Hydra cluster at University of Oxford. This work was supported by the Science and Technology Facilities Council Grant Number ST/W000903/1.

## DATA AVAILABILITY

The data underlying this article will be shared on reasonable request to the corresponding author.

## REFERENCES

- Abbott B., et al., 2019, *Physical Review X*, 9  
 Bahcall J. N., Wolf R. A., 1976, *ApJ*, 209, 214  
 Bartos I., Kocsis B., Haiman Z., Márka S., 2017, *ApJ*, 835, 165  
 Baruteau C., Cuadra J., Lin D. N. C., 2011, *ApJ*, 726, 28  
 Boeholt T. C. N., Rowan C., Kocsis B., 2023a, *MNRAS*, 518, 5653  
 Boeholt T. C. N., Vaillant T., Correia A. C. M., 2023b, *MNRAS*, 519, 3281  
 DeLaurentis S., Epstein-Martin M., Haiman Z., 2023, *MNRAS*, 523, 1126  
 Duffell P. C., D’Orazio D., Derdzinski A., Haiman Z., MacFadyen A., Rosen A. L., Zrake J., 2020, *ApJ*, 901, 25  
 Fabian A. C., Pringle J. E., Rees M. J., 1975, *MNRAS*, 172, 15  
 Gerosa D., Berti E., 2019, *Physical Review D*, 100

- Goldreich P., Lithwick Y., Sari R., 2002, *Nature*, 420, 643  
 Hansen R. O., 1972, *Phys. Rev. D*, 5, 1021  
 Heath R. M., Nixon C. J., 2020, *A&A*, 641, A64  
 Li R., Lai D., 2022, *Monthly Notices of the Royal Astronomical Society*, 517, 1602  
 Li R., Lai D., 2023a, *arXiv e-prints*, p. arXiv:2303.12207  
 Li R., Lai D., 2023b, *Monthly Notices of the Royal Astronomical Society*, 522, 1881  
 Li Y.-P., Dempsey A. M., Li S., Li H., Li J., 2021, *The Astrophysical Journal*, 911, 124  
 Li J., Lai D., Rodet L., 2022, *ApJ*, 934, 154  
 Li J., Dempsey A. M., Li H., Lai D., Li S., 2023, *The Astrophysical Journal Letters*, 944, L42  
 Mardling R. A., Aarseth S. J., 2001, *MNRAS*, 321, 398  
 McKernan B., Ford K. E. S., Lyra W., Perets H. B., 2012, *MNRAS*, 425, 460  
 McKernan B., Ford K. E. S., Kocsis B., Lyra W., Winter L. M., 2014, *MNRAS*, 441, 900  
 Miralda-Escudé J., Gould A., 2000, *ApJ*, 545, 847  
 Moody M. S. L., Shi J.-M., Stone J. M., 2019, *ApJ*, 875, 66  
 Mouri H., Taniguchi Y., 2002, *The Astrophysical Journal*, 566, L17  
 Muñoz D. J., Lithwick Y., 2020, *ApJ*, 905, 106  
 Muñoz D. J., Miranda R., Lai D., 2019, *ApJ*, 871, 84  
 Naoz S., 2016, *ARA&A*, 54, 441  
 O’Leary R. M., Rasio F. A., Fregeau J. M., Ivanova N., O’Shaughnessy R., 2006, *ApJ*, 637, 937  
 O’Leary R. M., Kocsis B., Loeb A., 2009, *MNRAS*, 395, 2127  
 O’Leary R. M., Meiron Y., Kocsis B., 2016, *ApJ*, 824, L12  
 Ostriker E. C., 1999, *The Astrophysical Journal*, 513, 252  
 Panamarev T., Shukirgaliyev B., Meiron Y., Berczik P., Just A., Spurzem R., Omarov C., Vilkovskij E., 2018, *MNRAS*, 476, 4224  
 Peters P. C., 1964, *Phys. Rev.*, 136, B1224  
 Quinn T., Perrine R. P., Richardson D. C., Barnes R., 2010, *The Astronomical Journal*, 139, 803  
 Rakavy G., Shaviv G., 1967, *The Astrophysical Journal*, 148  
 Rowan C., Whitehead H., Boeholt T., Kocsis B., Haiman Z., 2023a, in prep.  
 Rowan C., Boeholt T., Kocsis B., Haiman Z., 2023b, *MNRAS*, 524, 2770  
 Rozner M., Generozov A., Perets H. B., 2023, *MNRAS*, 521, 866  
 Safarzadeh M., Haiman Z., 2020, *The Astrophysical Journal Letters*, 903, L21  
 Samsing J., et al., 2022, *Nature*, 603, 237  
 Secunda A., Bellovary J., Mac Low M.-M., Ford K. E. S., McKernan B., Leigh N. W. C., Lyra W., Sándor Z., 2019, *ApJ*, 878, 85  
 Stone J. M., Tomida K., White C. J., Felker K. G., 2020, *The Astrophysical Journal Supplement Series*, 249, 4  
 Tagawa H., Haiman Z., Kocsis B., 2020, *ApJ*, 898, 25  
 Tang Y., MacFadyen A., Haiman Z., 2017, *MNRAS*, 469, 4258  
 Tiede C., Zrake J., MacFadyen A., Haiman Z., 2020, *ApJ*, 900, 43  
 Tory M., Grishin E., Mandel I., 2022, *Publications of the Astronomical Society of Australia*, 39  
 Vynatheya P., Hamers A. S., Mardling R. A., Bellinger E. P., 2022, *Monthly Notices of the Royal Astronomical Society*, 516, 4146  
 Westernacher-Schneider J. R., Zrake J., MacFadyen A., Haiman Z., 2022, *Phys. Rev. D*, 106, 103010  
 Westernacher-Schneider J. R., Zrake J., MacFadyen A., Haiman Z., 2023, *arXiv e-prints*, p. arXiv:2307.01154

## APPENDIX A: CONSTANT VISCOSITY

In this study, we adopt a homogeneous viscosity throughout the simulation domain. In real system, we expect viscosity to vary throughout the shearing box due to variations in the local sound speed  $c_s$  and compression of the minidisks vertically by the gravity of each BH. Li & Lai (2023a) adopt a reasonable prescription within their paper by prescribing a variable  $\Omega$  within the expression  $\nu = \frac{c_s^2}{\Omega}$  that considers BH contributions within the SMBH gravity field. However, we feel

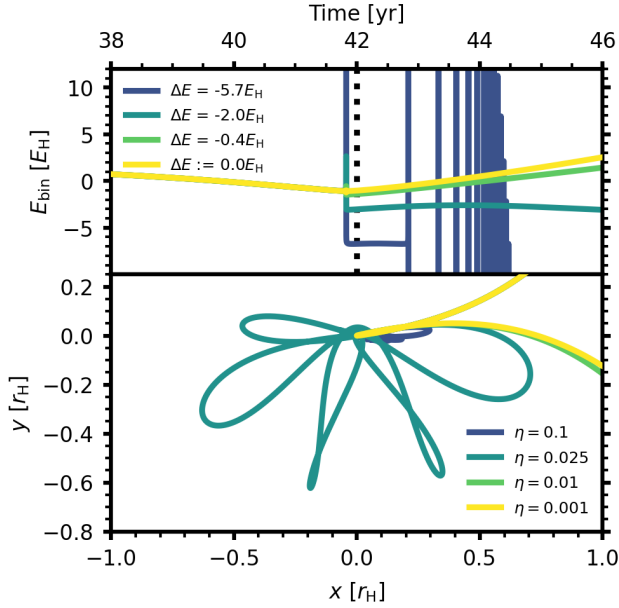


**Figure B1.** Comparisons of runs with  $b = 2.0r_H$ ,  $\rho_0 = 0$  with varying values for the timescale pre-factor  $\eta$ . In the lower panel, the path traced by the outer BH in a frame centred on the inner BH. In the top panel, the binary energy as a function of time including errors in energy. If  $\eta$  is too large, a significant energy error is generated during first close encounter. In the cases where  $\eta \geq 0.025$ , the error is so severe that a binary is spuriously formed. If  $\eta$  is reduced, this issue is not present. Energy errors  $\Delta E$  are calculated in comparison to the  $\eta = 0.001$  model at  $t = 42$ yr (marked by the dotted vertical line in the top plot)

that without a full treatment with more realistic heating and cooling physics, accurate predictions as to the thickness of the BH minidisks and therefore the size of turbulent vortices are impossible to make. Such physics are beyond the scope of this study and we instead adopt a homogeneous viscosity as a first-order approximation to a system that requires further advanced modelling to more accurately simulate.

## APPENDIX B: TEMPORAL CONVERGENCE

Careful study of our system at very low gas density and for very deep close encounters made clear the need for caution when attempting to resolve the motion of the BHs temporally. If an insufficiently small pre-factor  $\eta$  is chosen to scale the BH timestep (as introduced in Section 2.2), an error arises in the n-body integration during close encounter. Here, where the calculated timestep is too large, the binary system loses energy spuriously due to numeric effects, leading to the creation of a binary that should not exist physically. This pseudo-dissipation is most noticeable for systems with a very deep first periapsis; Figure B1 displays the energy error after first close encounter for runs with larger  $\eta$  values, as compared to the  $\eta = 0.001$  system. Investigation into convergence for such systems suggests that for this study,  $\eta \leq 0.005$  is sufficient, though we set  $\eta = 0.001$  for safety. For a more comprehensive study covering much deeper close encounters, a more stable integrator or smaller  $\eta$  value may be required.

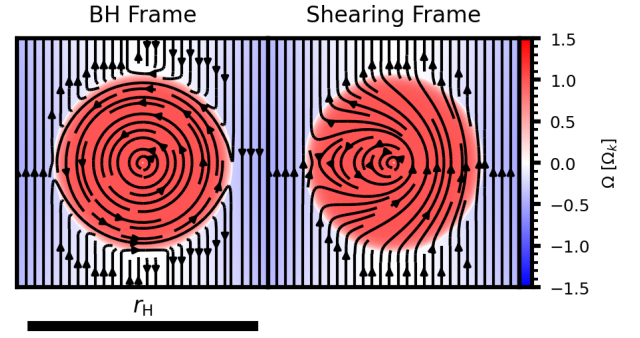


**Figure C1.** Velocity field near the inner BH at  $t = 0$ , displayed with streamlines in the BH frame (left) and shearing frame (right). The background colourmap displays orbital frequency about the BH in its own frame.

## APPENDIX C: SEEDING BLACK HOLES

As introduced in Section 3, our BHs are added impulsively to the disc at  $t = 0$ , as opposed to growing the BH mass steadily from zero. Without care, this can lead to expensive to resolve chaotic flows as gas falls directly onto each BH. To stabilise this early phase, we seed each BH within a distorted velocity field. We do not find this seeding to effect the late-time behaviour or outcomes and it is included mostly as a precaution. Under this routine, the true gas velocity field  $\mathbf{u}$  is dependent on proximity to the BHs.

$$\mathbf{u} = \begin{cases} \mathbf{u}_0 & r_n \geq r_d \forall n \\ \mathbf{u}_0 (1 - k_d) + k_d \mathbf{u}_{d,n} & r_n < r_d \end{cases} \quad (\text{C1})$$

where we interpolate between velocity fields for the background  $\mathbf{u}_0$  and for minidisc  $n$   $\mathbf{u}_{d,n}$  by a kernel  $k_d = 1 - \left(\frac{r_n}{r_d}\right)^{16}$  on a length scale  $r_d = 0.5r_{h,s}$ . Each of the velocity fields are represented as

$$\mathbf{u}_0 = \mathbf{u}_{\text{eq}} = \begin{pmatrix} 0 \\ -q\Omega x \end{pmatrix} \quad (\text{C2})$$

$$\mathbf{u}_{d,n} = \sqrt{\frac{Gm_n}{r_n^2}} \hat{\phi}_n + \mathbf{v}_n \quad (\text{C3})$$

Here the background field is the Keplerian shear of the AGN disc and the local velocity field matches Keplerian rotation around an isolated, mobile BH labelled  $n$ . This interpolated velocity does not match the steady-state velocity field reached once the minidisks have formed, but acts as a stabilising intermediary solution with an easy analytic representation. Figure C1 demonstrates this routine by displaying the velocity field near a BH at  $t = 0$ .

## APPENDIX D: NUMERICAL ISSUES

For a small subset of runs in the parameter grid, we experienced numerical errors arising from strong density gradients generated during the chaotic gas flows immediately after close BH encounter. This would lead to large nonphysical accelerations of single cells of gas. Multiple methods were attempted to treat this issue, involving a variety of different solvers, reconstructions, resolutions and integrators. It is possible that such instabilities could be resolved fully if the resolution were increased considerably near each BH, but this would lead to a computational cost unacceptable for this study. Ultimately,

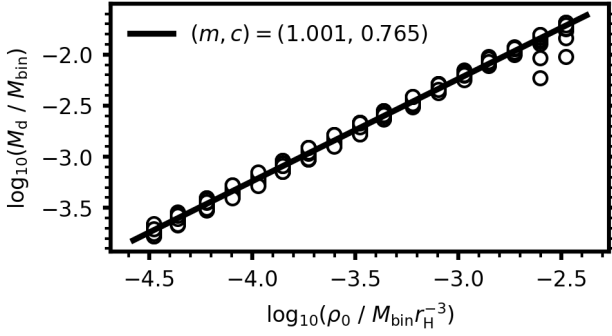


**Figure E1.** Linear relationship between the ambient AGN disc density and the approximate minidisc masses before close encounter for models with  $b = 1.8, 2.5r_H$ . There is some variation in disc mass between models with different  $b$  values at set densities, and some of the higher density systems feature under-massive minidiscs, but generally the fit holds well.

no one choice was able to eliminate 100% of the errors. As such, we were forced to adopt an "error-catching" routine that identified failing cells and smoothed out their hydrodynamical quantities with their neighbours. As only a single cell would fail in a single timestep, we believe this method prevented the arrival of such errors from affecting the large-scale behaviour of the hydrodynamical system. We do not expect the presence of such errors, or the corrective methodology implemented, to have any affect on the conclusions drawn by this study.

## APPENDIX E: MINIDISC MASS GROWTH

Given that each simulation evolves for a similar amount of time before close encounter (should one occur), we can predict the minidisc mass at interaction from the ambient AGN disc density. Figure E1 details the strong linear relationship between the ambient density and the gas mass within the Hill sphere of a single BH when the BHs reach within  $2r_H$  of each other. There is only a minor variance between simulations at different radial separations, due to slightly different travel times to intersection. We note that some models at high density have considerably less massive minidiscs, this is due to gas perturbing the BHs onto wide, fast moving trajectories which prevent significant gas buildup. This is generally inconsequential to the analysis presented in this paper, as such trajectories feature no close encounter.

## APPENDIX F: PREDICTIVE MODELLING ACCURACY

The framework presented in Section 6 provides a reasonably accurate (0.4dex) predictor of binary energy immediately after first periapsis given the binary orbital components are known at Hill intersection. The model itself performs better in certain areas than others: it struggles to accurately predict very deep periapsis encounters, and the energetic fitting from Equation (24) is a significant source of scatter. Figure F gives a complete breakdown of the errors introduced by each step of the fitting procedure.

## APPENDIX G: JACOBI REGIONS

While not the principle focus of this paper, we can inspect our grid of simulations for the existence of Jacobi interactions: narrow regions in impact parameter space where the SMBH is able to encourage multiple interactions between the black holes even without the presence of gas (Boekholt et al. 2023a). These interactions are identifiable as unbound systems with multiple interactions i.e. systems with a second periapsis within the Hill sphere. Such systems are highlighted in Figure G.

This paper has been typeset from a  $\text{\TeX}/\text{\LaTeX}$  file prepared by the author.

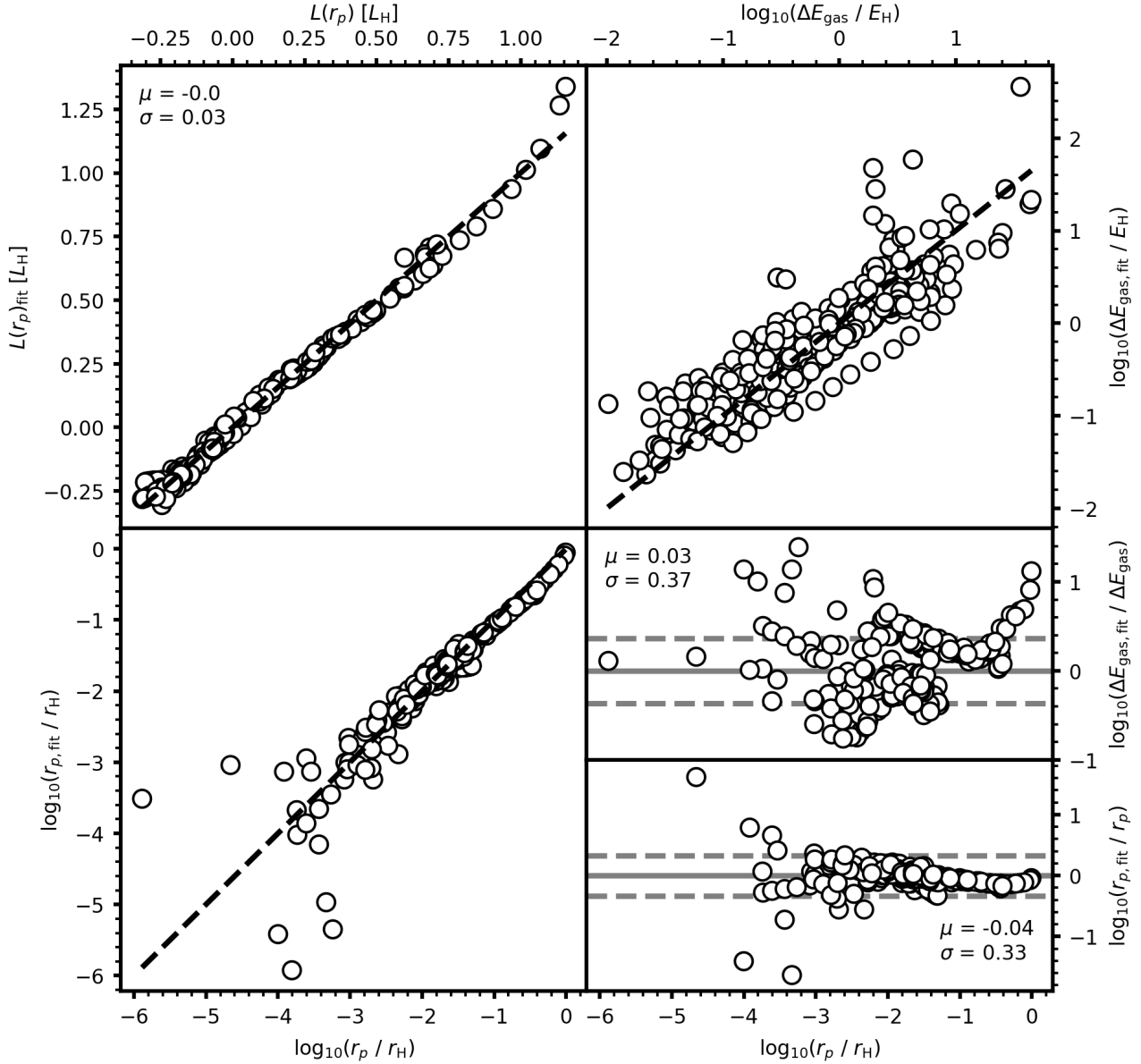


**Figure F1.** Fitting data for the predictive modelling sub-routines, for all 259 models that penetrate the mutual Hill volume. Top left panel: comparison of true angular momentum to that predicted by fitting from Figure 17, where the legend details the mean and spread in the error. Bottom left panel: comparison of true periapsis depth to that predicted by periapsis momentum and Equation (32). Top right panel: comparison of true gas dissipated energy to that predicted by full predictive modelling from the Hill quantities. Bottom right panels: residuals for upper right ( $\Delta E_{\text{gas}}$ ) and lower left ( $r_p$ ) panels, with  $1\sigma$  bounds as dashed lines. Energetic predictions by Hill intersection propagated values hold to on average 0.4dex, with the majority of scatter introduced by the power law fit from Equation (24). The predictor consistently overestimates the dissipation for very shallow encounters, likely due to the inaccuracy of Equation (32) for  $r_p \sim r_H$ . Note that these residuals are different from those presented in Figure 12, as in that method  $r_p$  was measured directly, whereas here it is predicted.



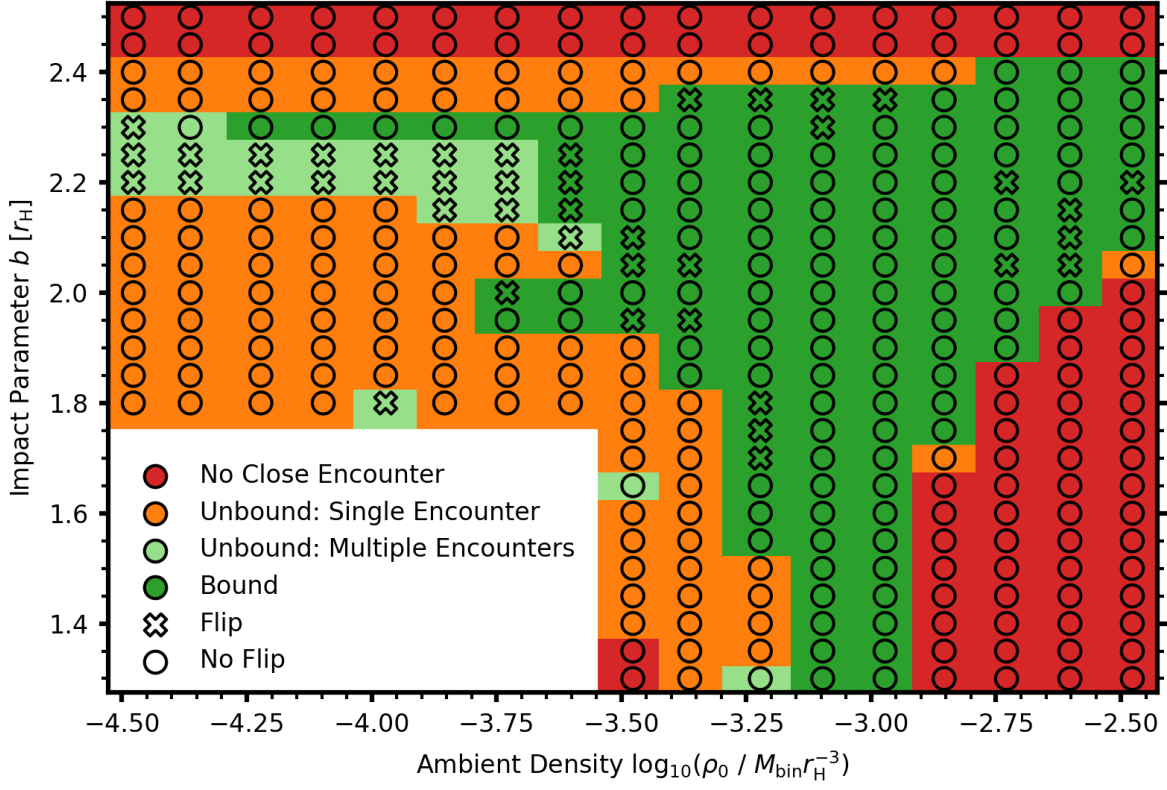


**Figure G1.** Number of close encounters between BHs for the full grid, where a close encounter is defined as a periapsis within the mutual Hill sphere. Jacobi encounters are visible around  $b = 2.15 - 2.3 r_{\text{H}}$  in light green within Region B (as defined in [Boekholt et al. \(2023a\)](#)), but also in a couple of systems around  $b = 1.6 - 1.8 r_{\text{H}}$  which are likely members of Region A. Region C is substantially narrower than the other regions, and likely lies beneath the sampling resolution in  $b$  used in this study (we might expect to see it around  $b = 2.45 r_{\text{H}}$ ). Inversion can also occur for bound systems near the zero angular momentum surface; these are not true Jacobi interactions (see Section 5.6)